Development of T1-thermometry for Monitoring the Skull during MRgFUS using a 3D Spiral Ultra-Short Echo Time Sequence

---

A Thesis

Presented to

the faculty of the School of Engineering and Applied Science

University of Virginia

---

in partial fulfillment
of the requirements for the degree

Master of Science

by

Yekaterina Gilbo

May 2020

APPROVAL SHEET

This Thesis
is submitted in partial fulfillment of the requirements
for the degree of
Master of Science

Author Signature: Yekaterina Gilbo

This Thesis has been read and approved by the examining committee:

Advisor: Craig Meyer

Committee Member: Wilson Grady Miller

Committee Member: John Mugler

Committee Member: _____

Committee Member: _____

Committee Member: _____

Accepted for the School of Engineering and Applied Science:

Craig H. Benson, School of Engineering and Applied Science

May 2020

Abstract

In MR-guided focused ultrasound (MRgFUS), acoustic waves are focused through the skull to destroy target brain tissue as a treatment for movement disorders. Bone attenuates ultrasound energy 20 times more efficiently than soft tissue [1]. Despite current clinical precautions such as circulating cold water around the scalp and predicting the cooling time needed for the skull between sonications from a model, a recent study has shown that MRgFUS led to unintended skull lesions in 7 out of 30 patients [2]. Current precautions are also incapable of limiting skull heating with off-center targets, and this discourages the use of MRgFUS for a wider variety of potential therapeutic targets, such as tumors. Furthermore, the cooling time estimate is not patient specific and can thus prolong an expensive, uncomfortable treatment needlessly. Thus, there is a need for skull thermometry.

Skull thermometry is challenging due to the extremely short T2* decay of cortical bone, which precludes the use of standard proton resonance frequency (PRF) methods, and because of the need for rapid imaging over a large field of view. Other researchers have shown a linear temperature dependence of T1 relaxation in cortical bone [3]. Our initial goal was to investigate the feasibility and repeatability of T1-weighted thermometry under various conditions, such as different magnetic fields, mechanisms of heating, and methods of analysis. Inconsistent results from T1-weighted thermometry led us to focus on investigating the repeatability of T1-mapping thermometry instead and to determine whether T1-mapping thermometry can be accelerated to meet clinical constraints.

Using a non-selective ultra-short-echo-time (UTE) 3D spiral sequence, we demonstrate that rapid T1 thermometry is feasible, and that it is more repeatable and quantitative than T1-weighted imaging.

Table of Contents

Chapter 1 General Introduction

1.1 MR-guided focused ultrasound

MR-guided focused ultrasound (MRgFUS) enables brain surgery with focused ultrasound (FUS) waves mechanically perturbing or heating brain tissue. The procedure is done by placing the patient's head into a FUS helmet composed of 1024 transducers. Each transducer is piezoelectric, converting current to sound waves through the vibration of crystals driving air oscillations. By computing the timing at which transducers need to turn on (phase delays) to focus the waves at a specific spot, a surgeon can destroy the targeted tissue to millimeter precision at ablative temperatures (55-60°C) with no damage to surrounding tissue and treat different disorders. An MRI is used to image the target and to determine the coordinates for the FUS system as well as to monitor the effect of the treatment through changes in T1, T2, and diffusion of the target [4]. For example, MRgFUS has been successfully applied to treat patients with essential tremor (ET). Patients with ET have a tremor typically affecting their hands and quality of life making functional activities such as drinking a glass of water, dressing, or writing very difficult [5]. Ablation of the thalamus in the brain helps to suppress the tremor observed during and immediately after the procedure. MRgFUS in the brain can also treat the symptoms of Parkinson's disease, neuropathic pain, and brain tumors [6]. Though MRgFUS is a rapidly growing technology in interventional radiology and functional neurosurgery, there remain many technical challenges to be solved so that MRgFUS can be a widespread treatment option for neuropathology [7].

Bone attenuates ultrasound energy 20 times more efficiently than soft tissue [6]. Heating of the skull during FUS therapy is thus a major concern limiting the amount of acoustic energy that can be safely transmitted into the brain and constraining which parts of the brain can be targets. Targets away from the center of the brain lead to more skull heating [1]. Despite current clinical precautions such as dropping the sound frequency to 650 kHz, making the FUS array larger to spread out the transmitted energy, and cooling the scalp actively with circulating water, there is still potential for injury [8]. A recent study has shown that MRgFUS led to unintended skull lesions in 16 out of 40 MRgFUS procedures [9]. Furthermore, skull heating may lead to nerve pain which impedes the treatment. Real-time skull thermometry would help validate proposed skull heating models and prevent unintended injury to patients. It would also potentially make treatment faster as surgeons wait 6-15 minutes for the skull to cool in between sonication during the three hour long treatment in which the patient is awake in the MRI and their skull is pinned to a frame. If the skull is shown to have returned to thermal baseline, the treatment can continue more quickly. Lastly, monitoring of skull heating would enable the development of MRgFUS for less central targets, such as for treatment of depression**. In this thesis, we focus on developing an MRI-based method to measure the skull temperature during treatment.**

1.2 Skull Physiology

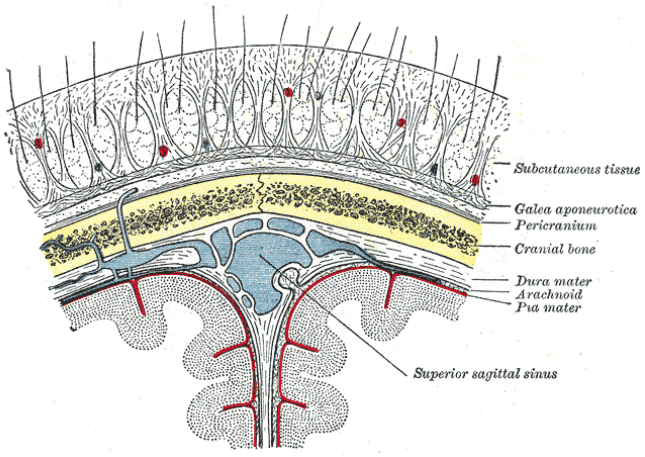

Figure 1 Diagrammatic section of the scalp, skull, and meninges from *Anatomy of the Human Body* by Henry Gray.

The skull has several important properties relevant for choosing MR sequence parameters. There is very little water in the skull (proton density) which decreases the amount of MR signal available requiring high SNR techniques. Water in the skull exists in two different forms as free water and bound water. Bound water has a very short transverse relaxation time (T2) on the order of ~100us. The echo time thus needs to be on the order of ~100us as well. The short T2 in solids like bone is a result of dipolar interactions between fixed nuclei as well as susceptibility effects, where nuclei are in two different fields and the signal rapidly dephases [10,11]. Conventional MRI is not fast enough to measure the transverse magnetization of bone before it decays away. Thus, we employ a UTE (ultra-short echo time) sequence originally developed to image the lungs [12].

As far as spatial constraints, on average, the skull is 5.58-8.17mm thick requiring good imaging resolution (≤ 5 x 5 x 5 mm) [13]. Its thickness varies from location to location and between patients. In order to capture skull heating in any location, a large field of view is needed, suggesting the use of a non-selective 3D sequence.

For temporal constraints, the skull's bone is similar to a ceramic material functioning as a thermal insulator preventing heat flow from the scalp into the brain and vice versa, and it has a cooling time constant estimated to be on the order of minutes [14]. This was also observed in a porcine model by McDannold et al [8]. Thus, we aim for a temporal resolution of ≤ 90s.

Table 1: Skull Thermometry Goals

Echo Time	Temporal Resolution	Spatial Resolution	FOV (3D)
$\leq 100us$	≤ 90s	≤ 5 x 5 x 5 mm	≥ 280 x 280 x 200 mm

Based on the above skull parameters and design constraints, we surveyed various methods of MRI thermometry and chose to investigate T1-weighted thermometry for rapid 3D skull thermometry.

1.3 MRI Thermometry

In MRI, the interactions between atomic nuclei are temperature dependent. Thus, MRI is well suited for non-invasive thermometry and is one of the main reasons MR guidance is used for focused ultrasound surgeries. Several MR physics parameters vary with temperature; T1, T2, and

the diffusion of coefficient of water all increase, while the resonance of frequency of hydrogen nuclei and proton density (polarization) decreases.

1.3.1 Proton Resonance Frequency Shift (PRF)

The most common method is based on the proton resonance frequency shift (PRF). When water molecules are tightly bound by hydrogen bonds, the electron clouds are less efficient at shielding [15]. As temperature increases, the hydrogen bonds between water molecules become looser leading to increased electron shielding of the hydrogen nuclei. The local magnetic field shielding leads to a decrease in proton resonance frequency by a consistent, high precision ($\alpha = 0.01\ ppm/°C$, or $1.2\frac{Hz}{°C}$ at 3T) for all tissues so that temperature changes can be quantified by measuring phase changes, $\Delta\phi$ [16]:

$$\Delta\phi = \phi(T) - \phi\left(T_{ref}\right) = \gamma\alpha B_o TE\Delta\mathrm{T} \qquad Eq.\ 1$$

B_o is the magnetic field, TE is the echo time, γ is the gyromagnetic ratio of hydrogen, and $\Delta\mathrm{T}$ is the temperature change. The consistent and universal change of the PRF thus makes it the preferred MRI thermometry method. However, PRF fails in bone. For UTE sequences (TE = 80us), the corresponding phase change for 5°C would be 0.19°, which is much too small of a phase difference to be detectable.

1.3.2 Proton Polarization

Proton polarization (density) depends on temperature through the Boltzmann distribution as thermal interactions jostle nuclei from alignment with the field:

$$P = \frac{N_\uparrow - N_\downarrow}{N} = \frac{1 - \exp(-\Delta\mathrm{E}/kT)}{1 + \exp(-\Delta\mathrm{E}/kT)} \qquad Eq.\ 2$$

where $\Delta E = \bar{h}\gamma B_o$. P is polarization, N is the number of non-integer spin protons (such as Hydrogen protons), $\Delta\mathrm{E}$ is the transition energy between aligned (up) and anti-aligned (down) protons, k is the Boltzmann constant, T is temperature, γ is the gyromagnetic ratio [15]. Polarization decreases with temperature, but the fractional change in temperature is too small ($0.3\%\ °C$) to be viable for bone thermometry.

1.3.3 Diffusion Thermometry

Brownian motion (diffusion) increases with temperature as:

$$D\ \approx e^{-E(D)/kT} \qquad Eq.\ 3$$

where D is diffusion, E(D) is the activation energy of molecular diffusion of water, k is the Boltzmann constant, and T is absolute temperature [17]. However, diffusion also requires a longer echo time due to the necessity of playing bipolar gradients, whereas bone imaging requires minimizing the echo time.

1.3.4 T2 Thermometry

T2, the transverse relaxation time, is caused by local magnetic field fluctuations due to movement of spins and random motion of neighboring molecules (spin lattice coupling) [15]. T2 is dependent on temperature through τ_C, the correlation time defined as the time a water molecule spends in any given position:

$$\frac{1}{T_2} = \gamma^2 B_{loc}^2 \left(\tau_C(T) + \frac{\tau_c(T)}{1 + \omega_0^2 \tau_c(T)^2} \right) \qquad Eq. 4$$

B_{loc} is the sum of the external B-field and field fluctuations. A shorter correlation time leads to a longer T2 [15]. Hotter spins lead to shorter correlation time leading to a longer T2. In clinical MRI, T2 has been shown to be linear with temperature, so that the temperature can be calculated [18].

However, T2 thermometry is difficult. To measure T2, a spin echo sequence is required, which increases the echo time (undesirable for bone imaging) as a π refocusing pulse must be played after the radiofrequency (RF) excitation pulse. The π pulse can be avoided if one is measuring T2* (with a spoiled GRE sequence) which includes dephasing due to magnetic field inhomogeneities and other factors such as diffusion. T2* changes with temperature are difficult to calibrate due to its sensitivity to environmental factors, such as field drift in the scanner. Both with T2 and T2* thermometry, several measurements must be acquired at different echo times while the signal is rapidly decaying. Additionally, T2* relaxation is not monoexponential as bone has a long T2* and a short T2* component requiring more measurements (up to 18 different echo times as shown by Huang et al.) [19-21]. Rapid 2D T2* thermometry has been demonstrated by Miller et al. in bovine bone [21, 22].

1.3.5 T1 Thermometry

T1 recovery results from dipolar magnetic field interactions between the two hydrogen protons in the same water molecule and also from inter-molecular interactions [15]. To relax from an excited energy state to a lower state, the system must transfer energy at field fluctuations near the Larmor frequency. The field fluctuations are characterized by the frequency spectral density, $J(w)$, which depends on motion as well. For example, free water exhibits fast motion and has a narrow $J(w)$, so its T1 values are long. As with T2, T1 is also dependent on correlation time

$$\frac{1}{T_1} = \frac{2\gamma^2 B_{loc}^2}{3} \frac{\tau_c(T)}{1 + \omega_o^2 \tau_c(T)^2} \qquad Eq. 5$$

For most MRI experiments, $\omega_o^2 \tau_c^2 \ll 1$, so that $\frac{1}{T_1} \propto \tau_c$. τ_c is also inversely proportional to temperature, so T1 also approximately increases linearly with temperature within the clinical regime [15]:

$$T = \frac{T_1(T) - T_1(T_{ref})}{m_1} + T_{ref} \qquad Eq. 6$$

A difficulty of T1 thermometry is due to the tissue dependence of m_1. Unlike the α constant from PRF which was tissue-independent, m_1 has high sample variability. T1 changes for not-fatty

tissue are not always reversible, especially if tissue coagulation occurs. However, T2 thermometry also has a variable tissue dependent factor m_2.

While T1 is less sensitive to the B_0-field of the scanner compared to T2* and does not require a refocusing pulse compared to T2, it is very sensitive to a non-ideal slice profile which occurs when the small flip angle approximation does not apply. If the slice profile is non-ideal, then the T1 measurements can be erroneous [22]. There are some methods for correcting for non-ideal slice profile, but they are still not fully reliable [23]. Thus, T2 thermometry may be better suited for 2D thermometry, but T1 thermometry is well-suited for 3D thermometry. Compared to the other methods, T1 based thermometry seemed most promising for skull monitoring. Several groups have demonstrated T1-based thermometry in cow bone taking two different approaches.

1.3.5.1 Prior work in T1-based bone thermometry

T1-weighted Thermometry

Miller et al. demonstrated **T1-weighted** localized signal reduction visually due to FUS in cow bone in 3D UTE images (2012, 2015) [24, 25]. Fielden et al. further demonstrated that the T1-weighted signal exhibits a linear decrease with temperature in a water-bath heated bone (2014) [26]. Contrary to Miller and Fielden's results, Ramsay et al. demonstrated an increase in T1-weighted signal in cow bone (rather than a decrease) in 2015 [27]. However, this group was not using a UTE sequence (TE = 1.05ms) and thus had T2-weighting implicit in their measurements, which could explain the opposite signal behavior. Odeen et al. also investigated temperature dependent changes in signal intensity and T1 in cortical cow bone and showed similar results to Miller and Fielden's results for their UTE sequence [28]. While work in T1-weighted thermometry seems promising, the repeatability of T1-weighted thermometry has not been investigated. Also, T1-weighted thermometry was not tested under clinical constraints, specifically the large FOV and short acquisition time **(Table 1).**

T1-mapping Thermometry

Han et al. demonstrated a T1 change with temperature in cortical bone with a linear coefficient between 0.67 and 0.84 ms/°C, on the order of 1-3%/°C (2015) [3]. However, their method required 8 min. of acquisition time, exceeding the estimated clinical constraint of 90s acquisition time. Miller et al. also showed a linear increase in T1 and T2 with temperature with 2D and 3D UTE in cow bone while developing a way to calibrate signal changes to temperature changes. Part of their results showed the problem with 2D T1-based thermometry due to non-ideal slice profile errors (2017, 2018) [21, 20]. T1-mapping has more potential to be repeatable and easier to calibrate, but suffers from requiring more acquisition time compared to T1-weighted thermometry.

1.4 General Hypothesis

Though T1-weighted thermometry may be difficult to calibrate with temperature as the signal can depend on many factors varying between experiments and treatments, it could indicate the binary presence of skull heating as well as when the skull returns to baseline temperature. Thus, our initial approach was to build on the T1-weighted thermometry of Miller and Fielden while adhering

to clinical constraints **(Table 1)** and to ultimately test the repeatability of the method with an ex-vivo human skull in addition to cow bone with different methods of heating. **In this thesis, I hypothesized that T1-weighted signal acquired with a volumetric spiral sequence decreases linearly with increasing temperature and can meet the clinical constraints from Table 1 in a repeatable way.**

1.5 Ultra Short Echo Time (UTE) Imaging

Bone is invisible in conventional MRI. In order to image and to perform thermometry on it, a UTE sequence is required so that the bone signal can be measured before it decays rapidly away. The difference between conventional imaging and UTE imaging is in the echo time, which is the time between the application of the RF pulse and the peak of the signal corresponding to the center of k-space, and in the duration of time measuring the signal [10]. Thus, UTE requires very short RF pulses on the order of ~100us and very fast sampling of k-space (before all of the signal decays away). If the readout is too long, this can result in resolution loss as the signal at high spatial frequencies is attenuated more by T2 decay.

Solutions to these constraints have been to use half-sinc RF excitations for selective excitation [29] or short hard rectangular pulses resulting in volumetric excitation. Both half-sinc RF pulses and hard rectangular pulses are very short. Short excitation pulses are also important because short T2 species relax during excitation, and if the pulse is too long, it is inefficient; magnetization might not be rotated to the nominal flip angle [10].

The readout is accomplished with either radial or spiral sampling. Radial trajectories are more widely used in UTE MRI due to an isotropic resolution in the x,y, and z directions and due to less signal loss during short readouts (<1ms). However, radial sampling has a longer acquisition time (up to 35x) than spiral sampling under the Nyquist sampling requirement [30].

1.5.1 UTE VIBE Sequence

We chose to investigate the UTE VIBE sequence for bone thermometry. The UTE VIBE sequence is a spoiled GRE sequence suitable for T1-based contrast imaging and is ultimately very fast. The UTE VIBE sequence was developed for breath-hold UTE lung imaging by Mugler et al. based on Qian and Boada's acquisition-weighted stack of spirals (AWSOS) for 3D UTE imaging. AWSOS uses a stack of spirals to accelerate in-plane data collection, variable-duration slice encoding, and a movable spiral readout achieving an echo time of 608us [31]. The main differences between UTE VIBE and AWSOS is that the UTE VIBE is non-selective with a rectangular RF pulse, and the min TE is less than 100us [12].

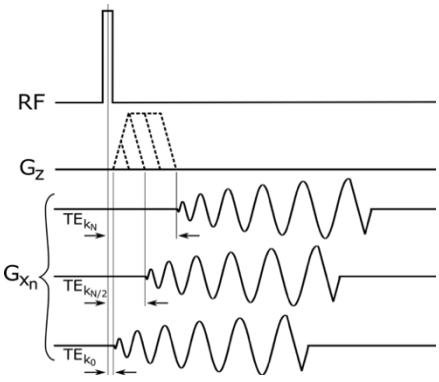

Figure 2. UTE VIBE Sequence. Image from Sam Fielden.

UTE VIBE has the following advantages for bone thermometry: (1) an ultra-short echo time limited only by the duration of a rectangular pulse; (2) a spiral readout enabling a highly efficient short

readout duration which starts at the center of k-space; (3) non-selective (3D) excitation. Also, it is a works-in-progress sequence for lung imaging that could be quickly implemented in the clinic.

Signal Model

The signal from UTE VIBE is modeled by

$$M_{xy} = S = M_o(T)\sin(\alpha)\frac{1 - e^{-T_1(T)/T_R}}{1 - \cos(\alpha)\, e^{-T_1(T)/T_R}} e^{-TE/T_2^*(T)} \qquad Eq.\ 7$$

where M_{xy} is the measured signal; $M_o(T)$ is the thermal equilibrium magnetization; α is the flip angle; T_R is the repetition time. The $e^{-T_1(T)/T_R}$ term provides the T1-weighting on the signal. If TE is sufficiently short, then the $e^{-TE/T_2*(T)}$ term is negligible (~1). $M_o(T)$ changes very minimally with temperature on the order of 0.3% per degree at temperature near room temperature (300K) [15]. Thus, the signal can be dominated by T1 changes. T1 can then be estimated by linearizing the equation above as shown in [32] or by using linear least squares fitting. The linearized form is

$$\frac{M_{xy}}{\sin(\alpha)} = E_1 \frac{M_o \cos(\alpha)}{\sin(\alpha)} + M_o(1 - E_1)e^{-TE/T2^*} \qquad Eq.\ 8$$

Where the slope $m = E_1$ gives T1. $T_1 = \frac{-TR}{\ln(E_1)}$. The two optimal flip angles are calculated by using propagation of errors to minimize an expression of uncertainty in quantitative VFA T1 mapping [22]. The optimal flip angles occur when the signal is 0.71 of the Ernst angle signal (maximum signal). However, solving for T1 from the linearized equation can lead to error in estimates, as a small change in slope will result in a large change in the T1 estimate. Thus, we used ordinary linear least squares (OLS) to find the best-fitting curve to the measured points by minimizing the difference between the model ($Eq.\ 7$) and the data.

1.5.2 RF Component

There are two ways to attain a short RF: using half-sinc excitation [29] or using a rectangular, non-selective pulse. However, if using half-sinc excitation, two half-sinc RF pulses are needed to achieve a good slice profile doubling scan time. UTE VIBE can attain a 120us rectangular pulse for a 35° flip angle (shorter for lower flip angles). The echo time with this kind of pulse is calculated from the center of the rectangular pulse with 20us for switching the coil from transmit to receive leading to a minimum 80us TE (60us+20us). The center of the rectangular pulse represents the average amount of T2 decay over time. The sequence also has an RF spoiler which prevents coherences from previous TR (stored in Mz) from contributing to the current TR's signal.

1.5.3 G_z Spatial Encoding

The G_z spatial encoding is one of the primary strengths of this sequence in minimizing echo time. Z-information is phase-encoded with a G_z gradient after the RF pulse and before the readout spiral. Each TR corresponds to a selected k-z plane in k-space, so that the third dimension is sampled traditionally in the Cartesian way, whereas k-space in k_x, k_y dimensions is sampled using spirals. Thus, the sampling trajectory is a stack of spirals. The area under G_z ($G_z\tau$, if the gradient is rectangular) selects for a specific k_z plane:

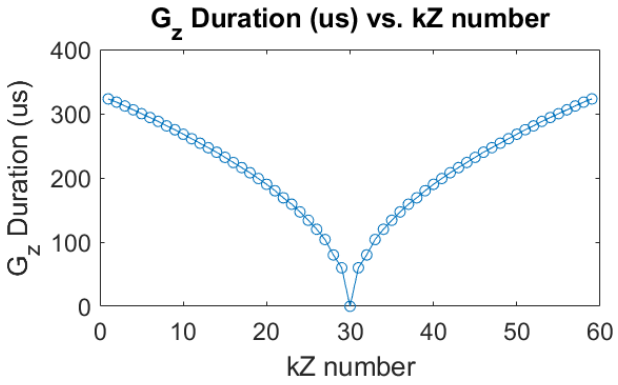

Figure 3. Gz Duration of the UTE VIBE vs kZ number. zRes = 5mm, zFOV = 30cm. Simulation from SpinBench.

$$k_z = \gamma G_z \tau. \qquad Eq.\ 9$$

Thus, the duration of the G_z gradients starts at $0\ us$ for $k_z = 0$ and increases to the maximum duration of 323us. The maximum duration and area are dependent upon the desired resolution:

$$k_{z,max} = \gamma G_{z,max} \tau_{max} = \frac{N}{\mathrm{FOV}_z} = \frac{1}{\Delta y} \qquad Eq.\ 10$$

By using the maximum gradient available on the scanner, τ, max can be calculated given the desired resolution. The incremental increase in area is determined by

$$\Delta k_z = \frac{1}{FOV_z} = \gamma \Delta G_z \Delta \tau, \qquad Eq.\ 11$$

where ΔG_z is set by the maximum slew rate.

1.5.4 Variable Echo Time

The echo time depends on the length of the Gz-phase encode gradient and is thus variable as described above and shown in **Figure 4**. Minimum echo time (minTE = 50us) occurs when there is no G_z gradient (at the center of k_z space); the readout spirals are played immediately after the RF pulse. For the GE-implemented version of the UTE VIBE, the maximum echo time is 373us for the highest kz plane of data. Because most of the signal energy comes from the center of k-space, the effective echo time is close to the minimum echo time. Variable echo time leads to blurring as the longer echo time corresponds to more T2-decay (attenuation) of the higher spatial frequencies **(Figure 5).** For species with a T2 of 450us as measured for cortical bone in [33], a blur of 0.6mm is predicted to occur for UTE VIBE which meets the goal for human imaging.

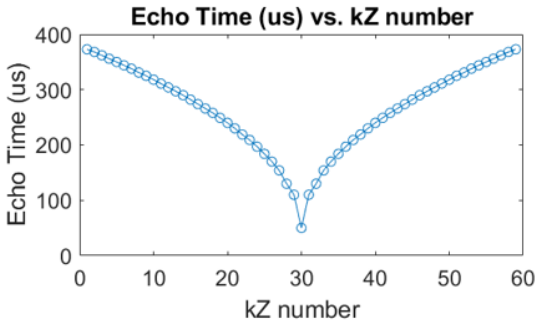

Figure 4. Echo Time vs. Kz. zRes = 5mm, zFOV = 30cm. Simulation from SpinBench.

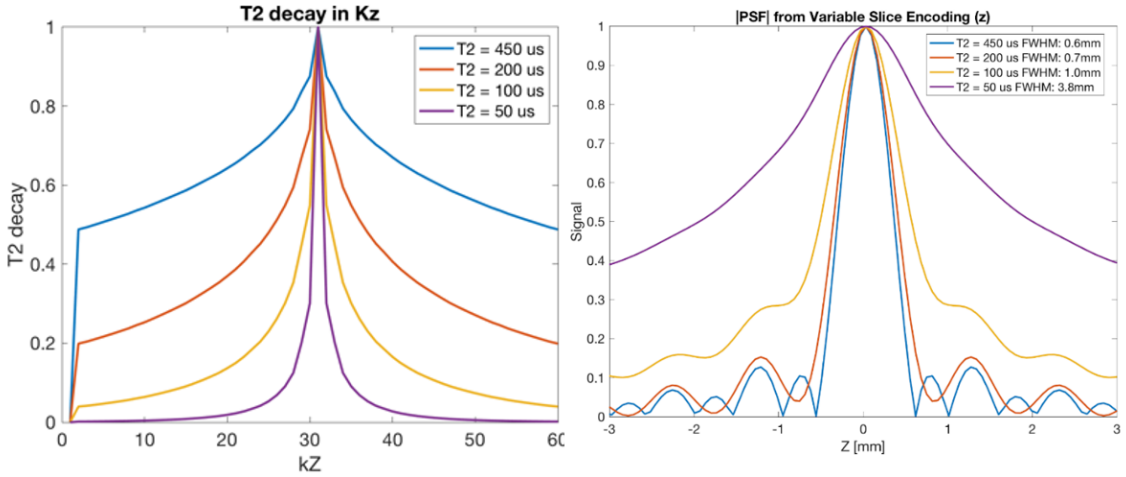

Figure 5. kZ dependent T2 decay leads to blur in Z. zRes = 5mm, zFOV = 30cm. Simulation from SpinBench.

1.5.5 Gx, Gy Spiral Readouts

Though spirals are technically difficult to implement on a scanner, require special reconstruction techniques, and are sensitive to off-resonance, they have many advantages, such as (1) reducing acquisition time due to efficient k-space coverage; (2) having a large SNR by starting acquisition at the center of k-space, which is also an advantage for ultra-short echo time sequences; (3) being robust against motion in dynamic MRI; (4) allowing real-time MRI with high in-plane resolution; and (5) being less sensitive to aliasing [34]. For these reasons, spirals are a good choice for bone thermometry, which requires ultra-short echo time, high SNR, and rapid image acquisition. The k-space spiral trajectory as implemented in the GE scanner is shown in **Figure 6**. To read more about spiral MRI (sampling requirement and gradient calculations), see the appendix (**A2**).

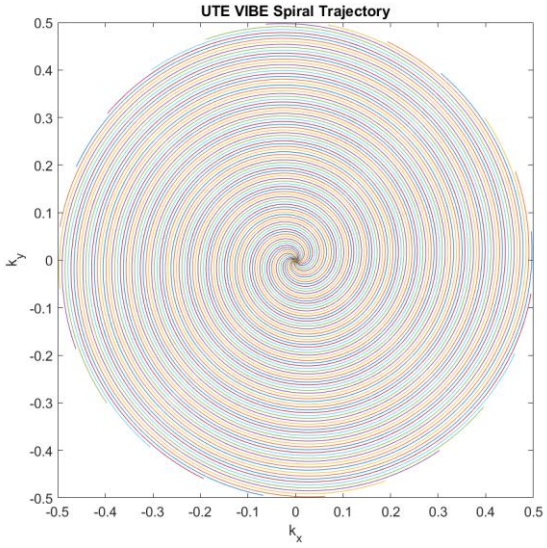

Figure 6. UTE VIBE K-space Trajectory (GE Scanner Implementation). Uniform spiral density.

1.6 Accelerated Thermometry

For clinical use, the thermometry of a patient's head in the water bath must not take more than 90s. Though initial goals detailed a coarse resolution (≤ 5 x 5 x 5 mm), a resolution of 1.9x1.9x5 mm is more reasonable for the average skull thickness of 6.5-7.1mm [7]. To achieve the 90s goal for two flip angles, the time per kz-encoding (200/5=40 kz encodings in total) must be 45s/40 = 1.13s per kz encode. Several acceleration methods were investigated.

1.6.1 Single Variable Flip Angle (sVFA) Acceleration

This method from Svedin et al. reduces scan time by half by acquiring the baseline temperature image at two flip angles and acquiring only the higher flip angle image for all the dynamic (hot) images [32]. T1 is then calculated under a false assumption that the reference low flip angle image does not change with temperature and then corrected using the spoiled GRE model.
sVFA was tested in a heating experiment (**Section 3.4**).

1.6.2 Partial K_z Acceleration

Partial Fourier imaging takes advantage of the conjugate symmetry of k-space applicable when the object is real or there are no phase errors, where $|k(x,y)| = |k(-x,-y)|$ and $\varphi_{x,y} = -\varphi_{-x,-y}$ (same amplitude, opposite phase). In theory, only half of k-space needs to be acquired, but in practicality, phase errors do occur from B_0-field inhomogeneities, concomitant gradients, and eddy currents [35]. Thus, partial Fourier sampling requires acquisition of 60% or more of k-space. For UTE VIBE, 6/8 kz partial Fourier sampling was selected, thus not collecting the bottom 25% of k-space and reducing scan time by ~25%.

1.6.3 Linear Variable Density Sampling Acceleration

Variable density spiral design samples the center of k-space at the Nyquist limit but under-samples the outer k-space regions reducing acquisition time. Because the center of k-space is fully-sampled and contains most of the energy, under-sampling in outer k-space leads to fewer artifacts than under-sampling uniformly [36]. As spiral aliasing results in blurring instead of replicant overlap, under-sampling in the high spatial frequencies can lead to benign artifacts.

Chapter 2 T1-weighted Thermometry

2.1 Experiment #1: UTE VIBE T1-Sensitivity Characterization

2.1.1 Methods

The sensitivity of the UTE VIBE sequence to T1-weighted signal changes was tested using a set of $NiCl_2$ phantoms. $NiCl_2$ is a paramagnetic contrast agent with a known relaxivity per concentration, $r_1 = 0.62\ (s^{-1} * mM^{-1})$ [37]. Seven concentrations of $NiCl_2$ were selected to match a set of desired T_1 values near that of cortical bone ($T_{1,\ baseline}$ = 120ms) using:

$$1/T_1 = 1/T_{1,dia} + r_1 C \qquad Eq.\ 12$$

T_1 is the target relaxation, $T_{1,dia}$ is the relaxation of diamagnetic host solution (water), C is the corresponding concentration of $NiCl_2$, and r_1 is the relaxivity per concentration of $NiCl_2$. The $NiCl_2$ was mixed with water in a capped plastic centrifuge tube.

An inversion recovery sequence (2D Turbo Spin Echo) was chosen to measure the T1 values of the $NiCl_2$ phantoms due to the relative accuracy of this technique.

Inverse recovery (IR) estimation of T_1 was performed by varying the inversion time (TI) and performing a NLSQ fit to a signal within a circular ROI:

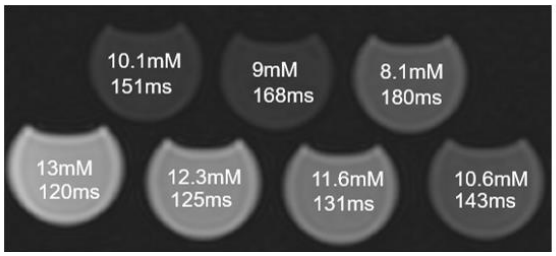

Figure 7: Example Image of $NiCl_2$ Phantoms

$$SI = M_{xy}(TI) = M_0\left(1 - 2e^{-\frac{TI}{T_1}}\right)e^{-TE/T_2} \qquad Eq.\ 13$$

T_2 decay in the above equation was negligible due to the short TE $(6.2\ ms)$ relative to the shortest (estimated) T_2 of $\sim 80ms$ for the highest concentration (13mM) of $NiCl_2$ [37].

After the "ground truth" value of T1 was measured with the more accurate IR sequence, the UTE VIBE was used to image the T1-weighted signal of the 7 different T1 phantoms at different flip angles to characterize the contrast sensitivity to T1.

Table 2

2D TSE Sequence Parameters (3T Prisma)			
Resolution (mm)	0.625x0.625x3	**Scan Time (min)**	2:33
FOV (mm^2)	160*160	**Number of Avgs**	1
TE (ms)	6.2	**Flip Angle (°)**	180
TR (s)	3	**Coil**	Head coil

2.1.2 Result

The sensitivity of the UTE VIBE was measured to be -0.4%/ms for the flip angle of 35° with a reasonable linearity ($R^2 = 0.99$) using the $NiCl_2$ phantoms (**Figure 8**). This data demonstrates that the UTE VIBE is sensitive to 10ms of difference in T_1 with a 5% change in signal, and the signal is linear with T_1. Rieke et Al. measured ~0.67%/ms [3]. Thus, the UTE VIBE should be able to resolve bone heating based on T1-weighted signal as the sequence is able to detect a 0.4%/ms change in T1.

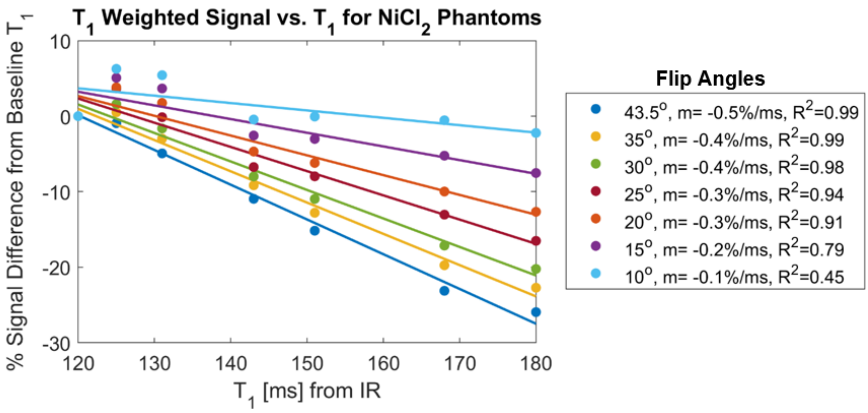

Figure 8. Measured T1-weighting Sensitivity for Different Flip Angles.

2.2 Experiment #2: Effect of ROI Selection and Field Strength in Water Bath Cooling in Ex-Vivo Cow Bone

2.2.1 Bone Preparation

Frozen cow femur was purchased and stored in refrigeration before the experiment. The bone was thawed at room temperature, and the marrow was removed. A fiber optic thermocouple was placed in a burr hole drilled into the cortical layer of each sample and in the water bath.

2.2.2 Water Bath Setup

In cooling experiments, each bone was placed in water at ~60°C, equilibrated for 10min., and then imaged with a 4-channel receiver coil placed on top of the sample during cooling.

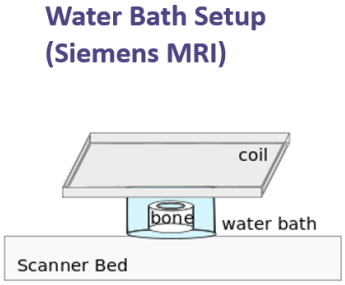

Figure 9

2.2.3 Results

Trial #1 - 1.5T

This experiment was conducted by Sam Fielden and formed the basis of this work [26]. The bone was submerged in water and imaged as it cooled with thermocouples indicating the bone temperature. With a large ROI (ROI-1 in red), the UTE (minTE = 50us) and the LTE (late TE, with minTE = 2.5ms) both showed the signal linearly decreased with temperature. It was expected that the LTE signal should not show a trend, as the bone signal decayed away rapidly and only water and fat contributed to the LTE signal. The presence of an LTE trend in ROI -1 indicates the ROI contains water, fat, or other longer T2 material. In the smaller ROI-2, the linear trend is no longer present in either the UTE or LTE signal. Thus, in ROI-1, the detected UTE trend may have been from non-bone material.

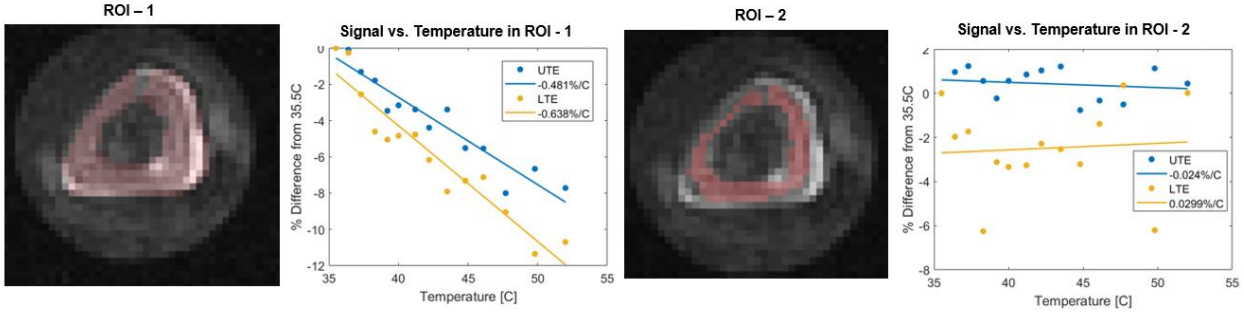

Figure 10

Table 3

3D UTE VIBE Sequence Parameters (1.5T Avanto)			
Resolution (mm)	2.7x2.7x3	**Scan Time (s)**	~78
FOV (mm^2)	256x256x96	**Number of Avgs**	1
TE (ms)	0.05/2.5	**Flip Angle (°)**	27
TR (ms)	11.6	**Coil**	4 channel flex coil
Readout (ms)	0.8		

Trial #2 - 1.5T

The experiment above was repeated by the author. A somewhat linear trend (0.29%/C) was detected, but it was quite noisy motivating the use of a higher magnetic field scanner. LTE data was not collected, and the data may also have fat or non-bone contamination.

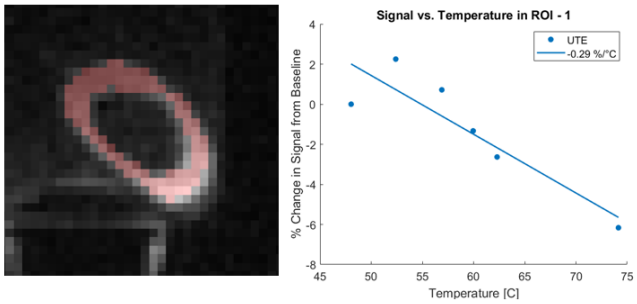

Figure 11

Table 4

3D UTE VIBE Sequence Parameters (1.5T Avanto)			
Resolution (mm)	2.67x2.67x3	**Scan Time (s)**	~78
FOV (mm²)	256x256x96	**Number of Avgs**	1
TE (ms)	0.05	**Flip Angle (°)**	27
TR (ms)	11.6	**Coil**	4-channel flex coil
Readout (ms)	0.8		

Trial #3 - 3T

The water bath experiment was repeated at 3T with UTE and LTE data collected. In ROI-1, a strong UTE and LTE trend was observed. However, the presence of LTE indicated partial volume effects from non-bone pixels in the ROI. A smaller ROI (ROI -2) showed almost no trend in UTE and very noisy data in LTE as would be expected for bone only pixels.

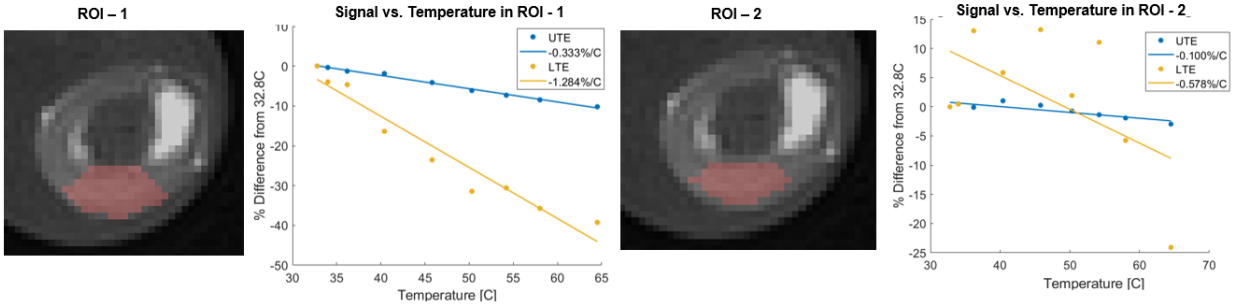

Figure 12

Table 5

3D UTE VIBE Sequence Parameters (3T Prisma)			
Resolution (mm)	2.13x2.13x3.43	**Scan Time (min)**	1:47
FOV (mm²)	204x204x137.2	**Number of Avgs**	1
TE (ms)	0.05/2.5	**Flip Angle (°)**	20
TR (ms)	11	**Coil**	4-channel flex coil
Readout (ms)	0.5		

2.2.4 Conclusions

The coarse resolution of these trials chosen in order to minimize imaging time presented the challenge of partial volume effects from non-bone (longer T2) materials. It was hypothesized this was due to the presence of fat, although this was not directly verified. Different selections of ROIs and the measurement of an LTE signal was helpful in identifying the origin of the signal.

RF Clipping Problem

After these experiments were conducted, it was realized that the actual flip angle as indicated in the DICOM files differed from the prescribed flip angle. A prescribed flip angle corresponds to a specific pulse amplitude for the specified pulse duration; however, the pulse amplitude has a maximum limit. Thus, when a flip angle of 35° was prescribed for a 50us TE, only a 20° flip angle was actually played due to RF clipping (maxing out of the system voltage). As shown **Figure 8**, a lower flip angle leads to lower sensitivity to T1-weighted changes (0.3%/ms vs 0.4%/ms). This problem was avoided later by manually checking the indicated voltage of the RF pulse and comparing with the indicated maximum voltage in the Siemens scanner.

2.3 Experiment #3: Effect of Heating by Small Animal FUS Transducer in 3T Avanto (Siemens) in Ex-Vivo Cow Bone

2.3.1 FUS Setup

In localized FUS experiments, each bone was placed on an ultrasound transparent film above a water tank of 1.1 MHz single element small animal transducer (FUS Instruments Inc.) The bones were targeted (1mm^3 focus) and ablated with a 45W continuous sonication six times for 135s to a temperature range between 30-70°C. Imaging was performed after each sonication and performed with UTE VIBE on the 3T scanners (Siemens Prisma and GE MR750).

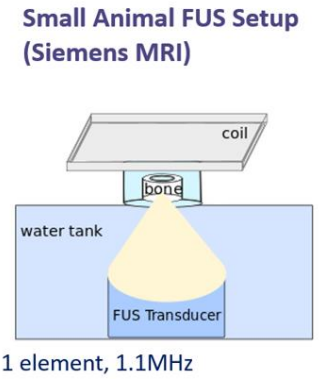

Figure 13

2.3.2 Results

Trial #1 - 3T

Compared to the control ROI, the target showed changes in the signal at the 50°C point. The signal was non-linear with temperature and the sharp change may have occurred from bone coagulation (cooking). The signal increased with temperature instead of decreasing with temperature as hypothesized from T1 of bone increasing with temperature. Thus, the signal change may be weighted by other factors, such as proton density or T2. The LTE data was very noisy indicating little or no presence of non-bone tissue.

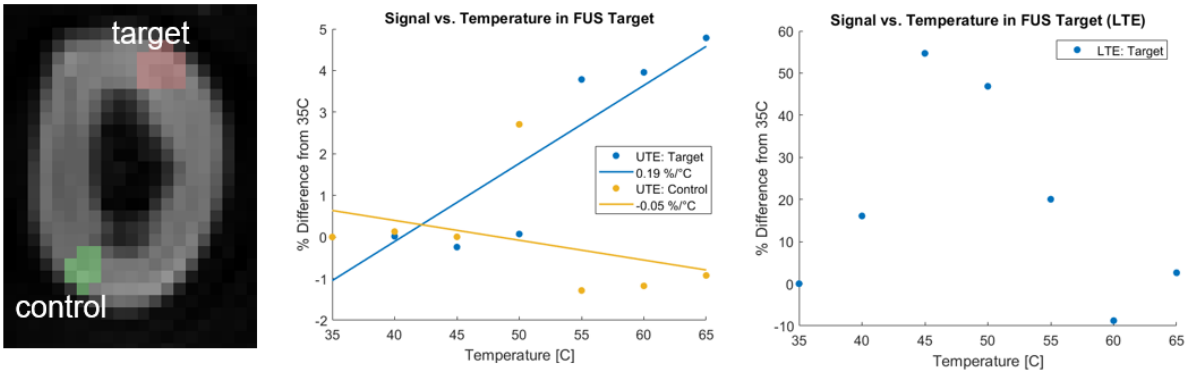

Figure 14

Table 6

3D UTE VIBE Sequence Parameters (3T Prisma)			
Resolution (mm)	2.27x2.27x3	**Scan Time (min)**	2:05
FOV (mm²)	217x217x120	**Number of Avgs**	1
TE (ms)	11	**Flip Angle (°)**	19
TR (s)	0.05/2.5	**Coil**	4-channel flex coil
Readout (ms)	0.5		

Trial #2 - 3T

The second trial showed that signal linearly increased with temperature once more contrary to expected results more in the target ROI than in the control ROI. The corresponding LTE data was very noisy suggesting the ROI included mostly bone pixels. The linear increase once again may have been due to unintended T2-weighting in the sequence.

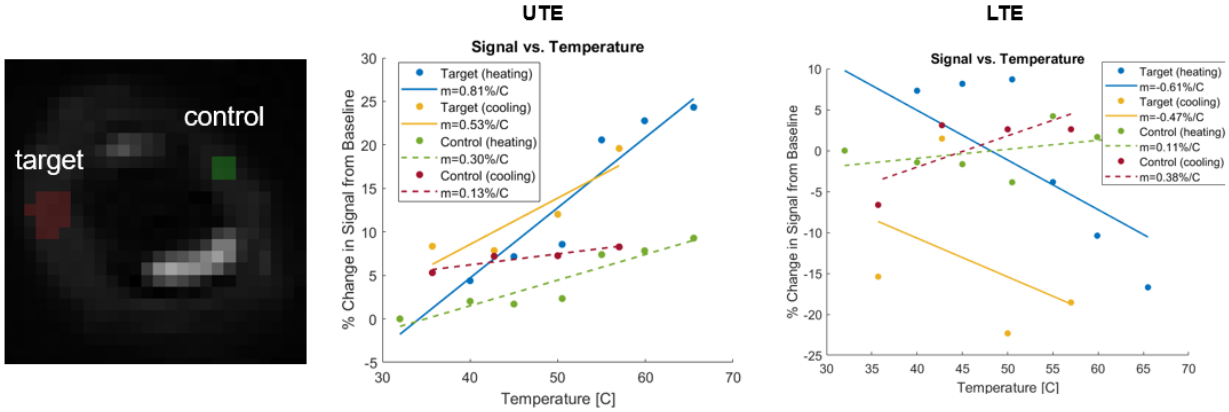

Figure 15

Table 7

3D UTE VIBE Sequence Parameters (3T Prisma)			
Resolution (mm)	2.125x2.125x3.42	**Scan Time (min)**	1:47
FOV (mm²)	204x204x136.8	**Number of Avgs**	1
TE (ms)	0.05/2.5	**Flip Angle (°)**	20
TR (s)	11	**Coil**	4-channel flex coil
Readout (ms)	0.5		

Trial #3 - 3T (w/Agar)

The third trial was conducted on bones poured into an agar mixture to decrease potential susceptibility mismatch between bone and air. The UTE trend (blue) showed the signal decreasing with temperature in the target more so than the control ROI; however, the LTE trend showed an even stronger decrease indicating potential partial volume effect from agar. A sharp transition at ~47°C again appeared in the UTE and LTE signal indicating potential coagulation occurring (**Figure 16**).

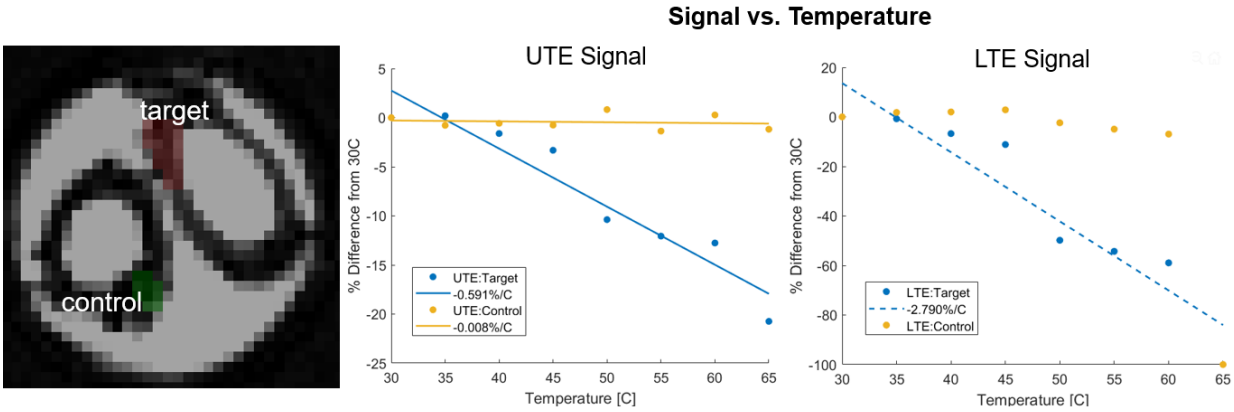

Figure 16

Subtracting the images at different temperatures helped visualize where the heating occurred. It is difficult to isolate the bone heating from the agar heating signal, but it appears that the bone showed a change in signal due to heating below.

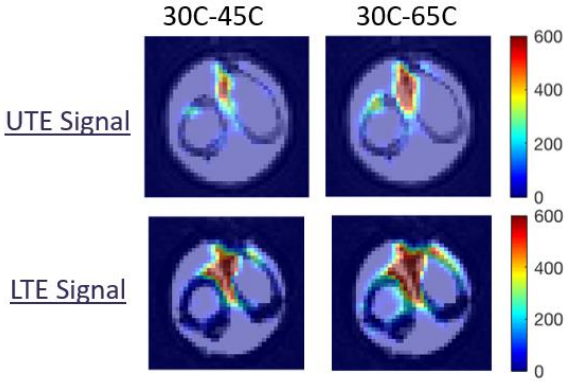

Figure 17

Table 8

3D UTE VIBE Sequence Parameters (3T Prisma)			
Resolution (mm)	3.01x3.01x3	**Scan Time (min)**	2:00
FOV (mm²)	289x289x51	**Number of Avgs**	1
TE (ms)	0.05/2.5	**Flip Angle (°)**	19.41
TR (s)	11	**Coil**	4-channel flex coil
Readout (ms)	0.5		

2.4 Experiment #4: Effect of Heating by Clinical FUS Transducer in 3T MR750 (GE) in In-Vivo Pig Skull

2.4.1 Clinical FUS Setup

Another lab member (Steven Allen) was conducting diffusion experiments on an in-vivo live porcine model with an Insighted ExAblate 1024 element (650 kHz) FUS Transducer and a GE MR750 Scanner. At the end of his experiment, a baseline UTE VIBE thermometry scan was done. Apodization was turned on to 97% so that the FUS was concentrated around the skull. Then, the pig was sonicated at 30W for 30s and re- sonicated every 15s during a three minute imaging sequence. The skull cooled for two minutes, and a post-sonication thermometry scan was acquired.

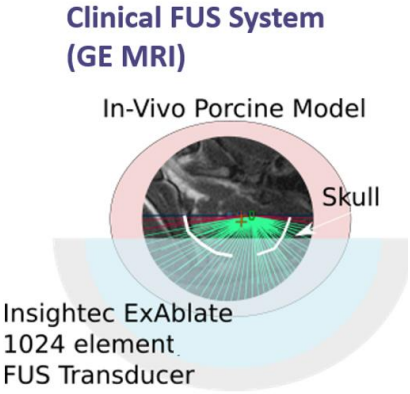

Figure 18

2.4.2 Results

Trial #1

Signal from an ROI in the skull was observed pre-sonication, during sonication, and post-sonication. For Trial 1, the signal decreased by 12% during sonication. In the subtraction images, we observed skull heating (UTE) and heating of the tissue (LTE) next to the skull. The UTE-LTE subtraction still showed a 4% difference in signal (post-sonication – during sonication). The presence of a strong LTE signal indicated partial volume from non-bone pixels. However, the UTE vs LTE images below suggest bone signal decreased from heating.

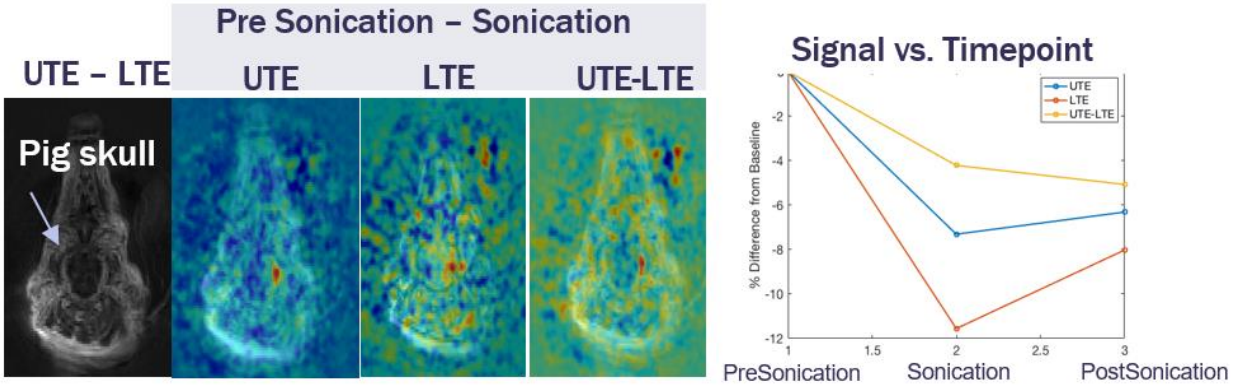

Figure 19

Table 9

3D UTE VIBE Sequence Parameters (3T MR750)			
Resolution (mm)	2.76x2.76x5	**Scan Time (min)**	2:15
FOV (mm^2)	300x300x295	**Number of Avgs**	1
TE (ms)	0.05	**Flip Angle (°)**	26
TR (s)	11	**Coil**	1CH ProtonTR

Readout (ms)	0.5		

Trial #2

In trial 2, the pig skull was smaller and the image quality decreased. Still, signal changes were observed in the skull with ~3% difference from baseline.

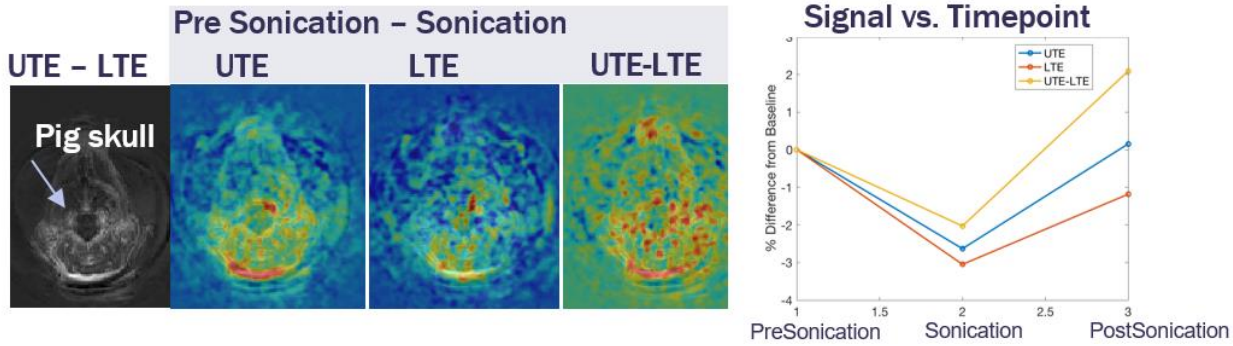

Figure 20

Sequence parameters were the same as in **Table 9** above.

Trial #3

In trial 3, heating in the skull (UTE) and heating next to the skull (LTE) were observed.

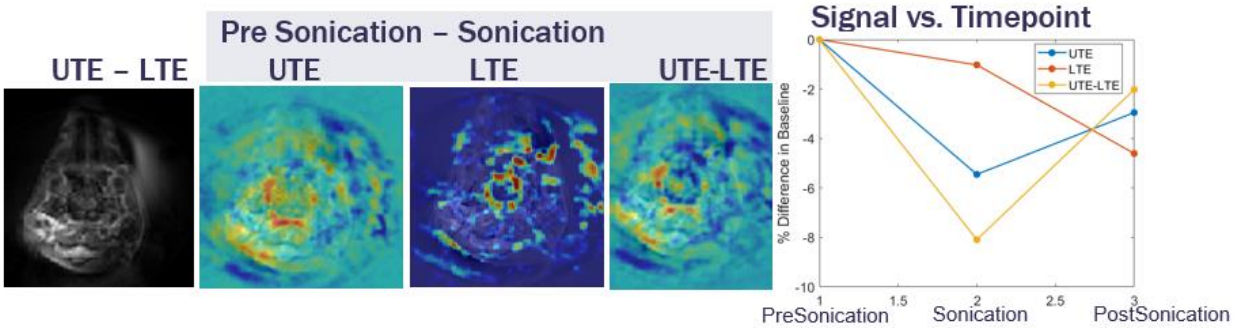

Figure 21

Sequence parameters were the same as in **Table 9** above.

2.5 Overall T1-weighting Thermometry Conclusions

Sometimes T1-weighting thermometry appeared to work, but was non-linear and inconsistent. It was sometimes insightful, as in the case of the pig skulls. Decreasing T2 weighting would improve the results, but currently the inconsistency of the trend makes the method difficult to further develop for clinical use. Thus, we turn toward T1-mapping thermometry at the cost of doubling the number of data acquisitions.

Chapter 3 T1-mapping Thermometry

3.1 Hypothesis

Though T1-mapping thermometry requires twice as many acquisitions as T1-weighted thermometry, the T1 vs. temperature trend should be much more reliable and linear. By using the advantages of spiral MRI, it is possible to accelerate T1-mapping to meet the clinical constraints (**Table 1**).

3.2 Experiment #1: UTE VIBE T1-Accuracy Characterization

3.2.1 Method

The T_1 mapping accuracy of the UTE VIBE variable flip angle method (VFA) was tested by using a $NiCl_2$ phantom. T_1 was initially measured using an inversion recovery (IR) 2D turbo spin echo sequence (TSE) to provide a ground truth comparison with VFA.

Table 10

UTE VIBE Sequence Parameters (3T Prisma)			
Resolution (mm)	1x1x5	**Scan Time (min)**	2:02
FOV (mm^2)	160x160x100	**Number of Avgs**	1
TE (ms)	0.05	**Flip Angle (°)**	10-45
TR (s)	11.7	**Coil**	32-Ch head Coil
Readout (ms)	0.5		

3.2.2 Result

T_1 values from the UTE VIBE VFA method and the IR method were compared in **Figure 23**. The IR values (in black) were closer to the expected T_1 based on $NiCl_2$ concentrations (mM). The mean difference in T_1 between VFA and IR was 6.39ms (4.46% difference). The VFA values in blue) are less linear. However, IR is not practical for UTE imaging; in IR, a 180° magnetization inversion must be achieved. Materials with short T2 such as cortical bone undergo relaxation during the inversion pulse thus making IR inefficient [11]. The noisy VFA-T1 measurements could be corrected by performing a B_1 map to measure the actual flip angles rather than relying on the potentially erroneously prescribed flip angles. Overall, the UTE VIBE VFA method was shown to be sensitive to T_1 with 5% error.

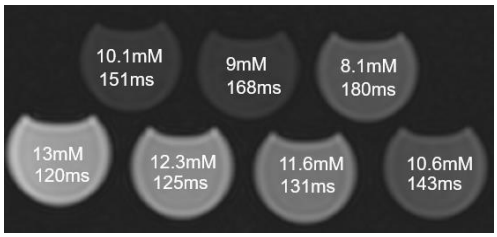

Figure 22. Example Image of $NiCl_2$ Phantoms Imaged by IR (IR = 110ms)

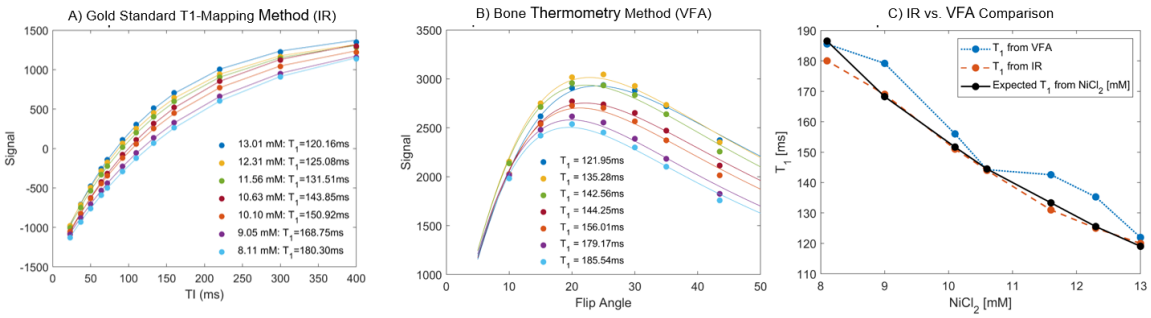

Figure 23. Characterizing the Accuracy of the UTE VIBE (VFA) to T1 changes. 1C) shows that T1 values from the IR method follow expected values from the $NiCl_2$ concentrations. VFA is less consistent with a mean difference of 5.47ms (3.56%) from expected T1 and 6.39ms (4.46%) from IR T1 values.

3.3 Experiment #2: T1-weighted Thermometry vs. T1-mapping Thermometry

3.3.1 Methods

Water Bath Cooling

Several changes were made with the previous water bath setup. The bone was placed into a small plastic container filled with water heating to ~70C and equilibrated for 10 min. The long axis of the bone was aligned with B_0 field of the scanner to minimize susceptibility effects and imaged transaxially with an L7 coil (diameter of 7cm) as it cooled, with an improvement in SNR due to the proximity of the coil to the sample.

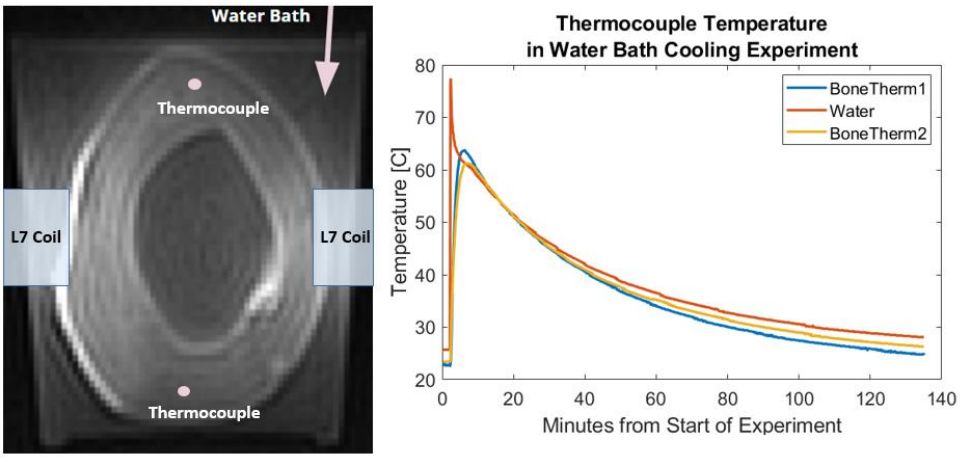

Figure 24. Water Bath Cooling.

Heating by Water Heater

Hysteresis of bone heating was tested by imaging the bone during heating using a water heater and a pump to see whether the change in T1 during heating was comparable to the change in T1 during cooling. A custom setup built by Wilson Miller was used as shown in **Figure 25**. The bone was placed into a small jar closed off from the outer jar. The circulated water was heated from room temperature up to 53°C in ~$4°C$ increments. The bone and water in the small jar slowly heated in response to the surrounding water leading to gradual temperature changes (yellow

trend slowly increases compared to the grey spikes of the circulating water in **Figure 25**). In order to fit the small bone jar, a drill press was used to cut the bone into a smooth round shape which allowed it to fit into the jar.

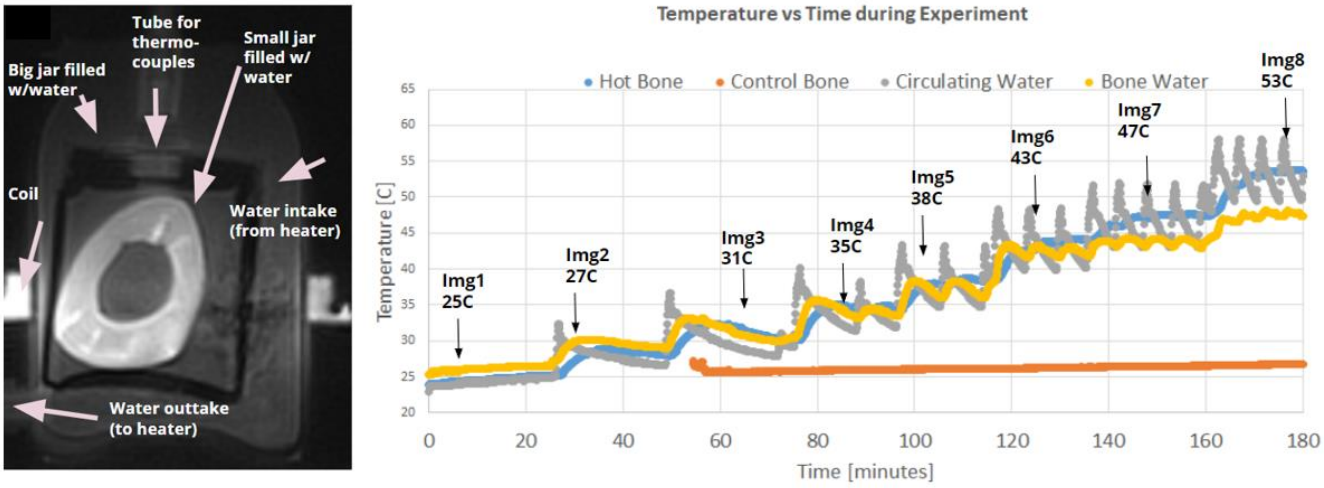

Figure 25. Heating of Bone with a Heater and a Pump

Table 11: Imaging Parameters

UTE VIBE Sequence Parameters (3T Prisma)			
Resolution (mm)	1x1x3	**Scan Time (min)**	1:44 (2.08s/slice)
FOV (mm²)	160x160x150	**Number of Avgs**	1
TE (ms)	0.08	**Flip Angle (°)**	8, 20, 44
TR (ms)	11.7	**Coil**	L7 + S5 + S6
Readout (ms)	0.5		

3.3.2 Results

Trial #1

Ex-vivo bovine femur bone was placed in a container of hot water and imaged as it cooled with a thermocouple measuring temperature in the bone. The signal was measured for three different flip angles (8°, 20°, 43.5°) at each temperature point. As T_1 increases with temperature, the T_1 weighted signal should decrease linearly in accordance to $Eq.7$ for all flip angles. As shown in **Figure 8**, the 8° FA data would show a smaller slope compared to the 43.5° FA. However, in the results below, a mix of trends was observed.

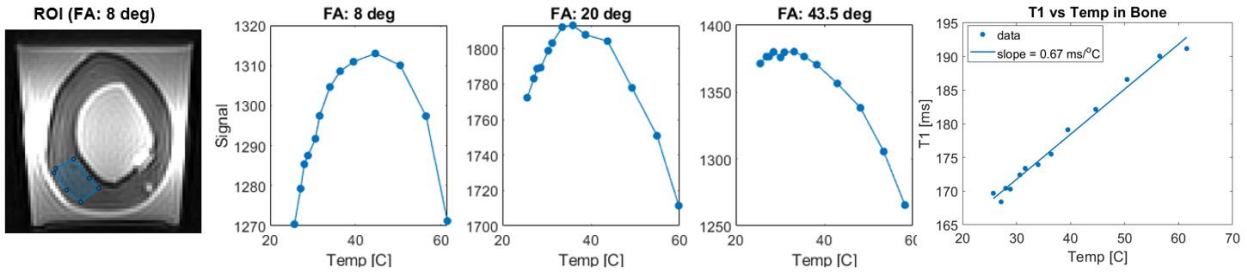

Figure 26. T1-weighted Signal vs. Temperature in Cow Bone. The signal behavior with temperature is nonlinear, even at higher flip angles (43.5°).

Trial # 1-5 Summary

To test T1-mapping thermometry, several trials both with heating bone and cooling bone in a water bath were conducted. The T1-weighted signal (at 35° flip angle) are shown in **Figure 27**. The T1 measured from the same ROI (same color) using two flip angles from the VFA method are shown in **Figure 27**b. Though the T1-weighted signal is nonlinear, the corresponding T1 vs temperature values are linear, increasing with temperature (average slope of 0.98 +/- 0.15 ms/°C), which is comparable to Han et al.'s result of 0.84 ms/°C measured using a slower 3D radial UTE pulse sequence [3].

The challenge of T1-mapping is that at least two flip angles of data must be acquired per temperature point doubling acquisition time. Thus, to make absolute T1 thermometry viable, acceleration techniques must be employed.

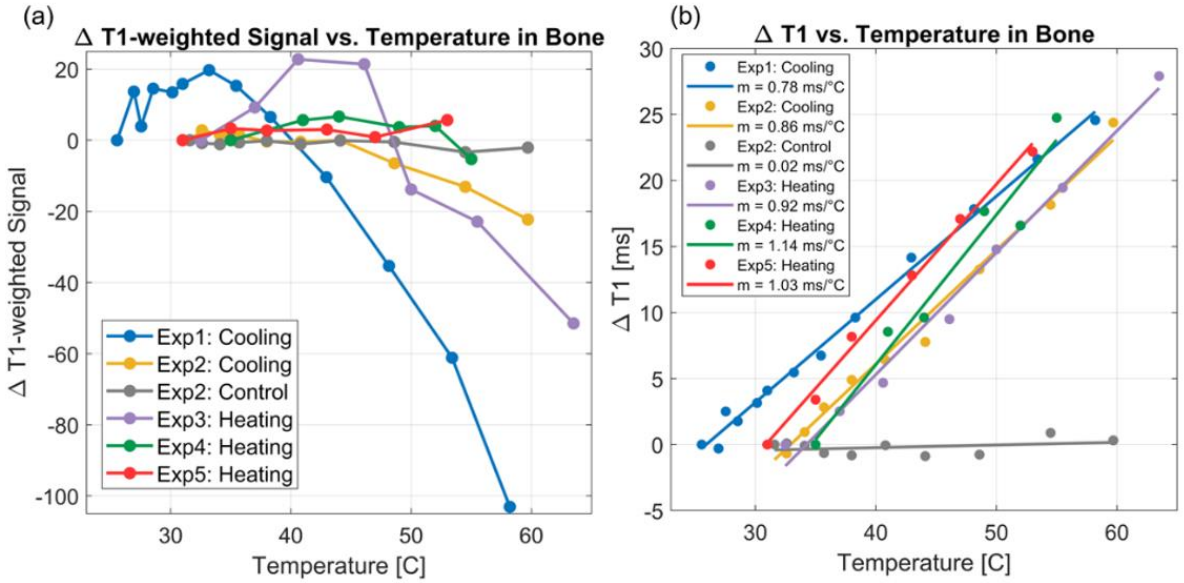

Figure 27. T1 weighted thermometry vs. T1 absolute thermometry. A) T1-weighted signal vs. temperature is inconsistent in its dependence on temperature. B) For the same bone sample and ROI, the T1 absolute value is consistently linear with temperature (m_{ave} = 0.98 +/- 0.15ms/°C).

3.3.3 Discussion

It appears that even though a UTE (TE = 80us) sequence was used, there may be significant amount of T2 weighting dominating at lower flip angles (FA: 8°) and being less prominent but still problematic at higher flip angles (FA: 43.5°). The potential effect of T2 was modeled below (**Figure 28**).

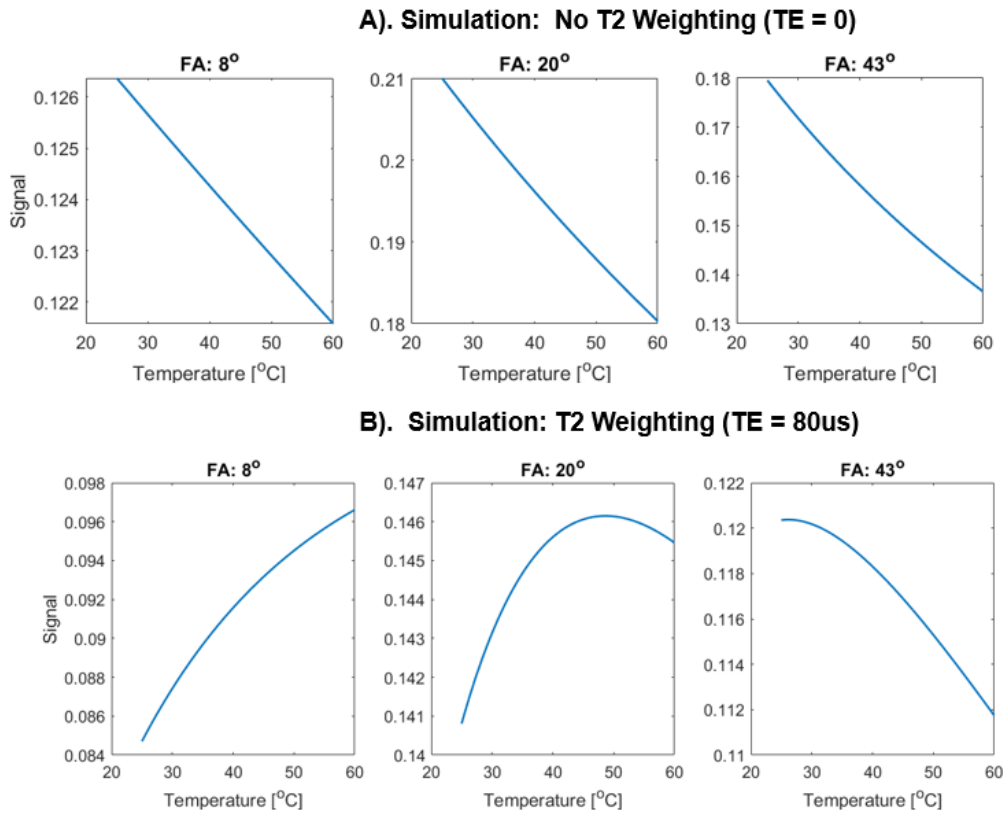

Figure 28. Simulated Signal vs. Temperature with T1 and T2 Weighting. A) Simulation parameters: T1 (25C) = 120ms [21], T1/Temp = 1.2 ms/C [21], TE = 0ms, TR = 11ms. B) Additional simulation parameters: T2 (25C) = 0.2 ms, T2/Temp = 4 ms/C from [21], TE = 80us.

Without T2 weighting, the signal vs. temperature for the flip angles of $8, 20, 43$ ° would look like **Figure 28 (A).** With T2 weighting (parameters extrapolated from previous work, the echo time and T2 (25C) was changed to match measured data), the signal model is no longer linear with temperature **Figure 28 (B).**

The simulation with T2 weighting though based on estimated parameters and not necessarily accurate indicates that T2 weighting could produce the measured results of **Figure 27**. The pattern of non-linear signal vs. temperature results in **Figure 27** was observed over 5 experiments leading to the conclusion that T1-weighted thermometry is not reliable for the UTE echo time of 80us potentially due to the non-negligible effect of T2 weighting. Decreasing the echo time to decrease T2-weighting is difficult as we run into B1 max amplitude issues; in order to decrease the TE, the RF pulse must be shortened. However, the RF pulse has a max B1 amplitude. Shortening the duration of the pulse necessitates decreasing the prescribed flip angle, which leads to increased T2 weighting.

3.4 Experiment #2: Single Variable Flip Angle (sVFA) Acceleration

In the case of $NiCl_2$, the sVFA method without any corrections (using the same reference image for the lower flip angle signal for all temperatures) led to an overestimated T1 vs. Temperature (yellow) compared to the regular VFA measurement (blue) (**Figure 29**). Svedin et al's model based correction did not work perfectly but did reduce the overestimation. For $NiCl_2$, a more careful application of sVFA would probably bring sVFA measurements closer to the VFA measurements as demonstrated in [32]. However, the sVFA method (with or without model based correction) did not produce a slope similar to the full VFA method for bone. This may be due to neglect of T2 weighting in the method, which is negligible for $NiCl_2$ but not negligible for ultra-short T2 bone as the sVFA method neglects T2 effects.

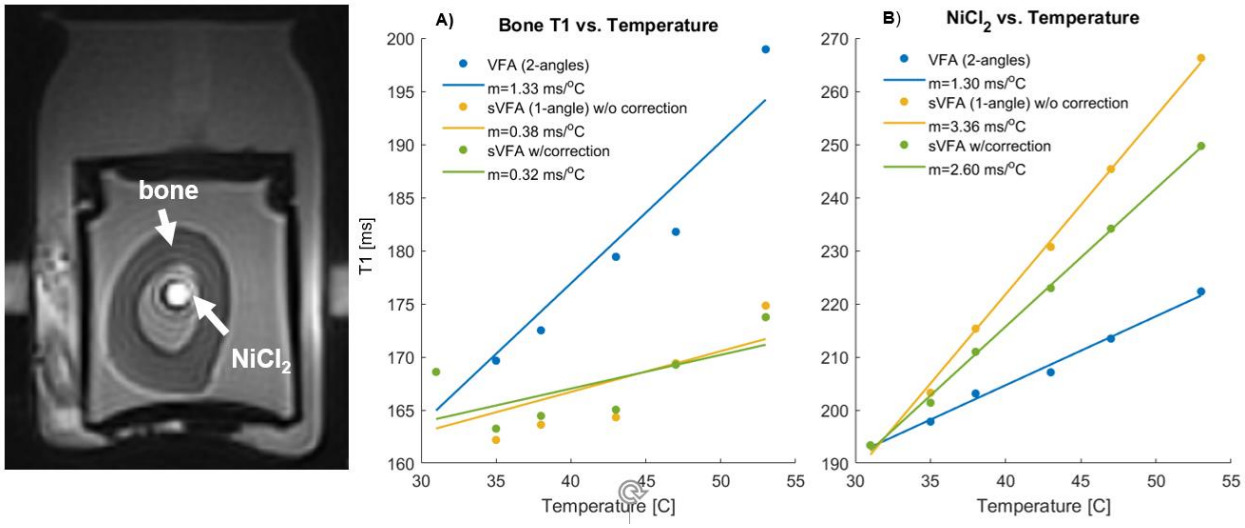

Figure 29. sVFA Acceleration Study. A) For bone nominal VFA (blue) shows T1 has good linearity and slope with temperature. The sVFA results (green, orange) show a much smaller slope and underestimate the T1. B) For $NiCl_2$ nominal VFA shows good linearity and slope. sVFA without correction (orange) overestimates T1 especially at higher Temperatures. sVFA with correction decreases overestimation but not completely.

3.5 Experiment #3: Partial K_z and Linear Variable Density Sampling Acceleration

A cooling experiment was conducted for cow bone cooling in a water bath with an under-sampled UTE VIBE sequence. A linear density was chosen (1.1 to 0.7) with 6/8 partial kz, 105 interleaves, (1.625, 1.625, 5mm) resolution leading to a 1.11s/kz-encode time (<90s for two flip angles). A linear T1 trend was observed with reasonable bone T1 values (**Figure 30**). Previous sequences (**Figure 27**) had a TA of 7.71s/slice with higher resolution; an acceleration by ~7 times still allows for a measurement of linear T1 changes. Thus, T1-VFA based thermometry is feasible with spiral variable-density acceleration. The slope of T1 vs. temperature for this under-sampled bone image is much higher than previous measurements (averaging 0.98 ms/°C). The effect of under-sampling on the measured change of T1 with temperature in cow bone remains to be investigated

and would provide insight on how under-sampling may affect the calibration of T1 changes with temperature.

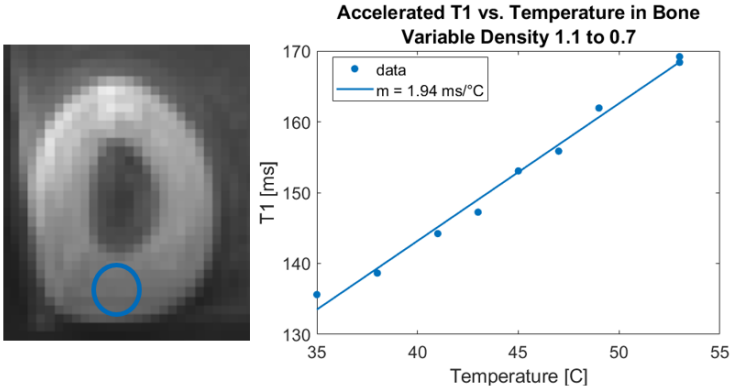

Figure 30. Variable Density, Partial Kz Acceleration Test in Bovine Cortical Bone.

Table 12

UTE VIBE Sequence Parameters (3T Prisma)			
Resolution (mm^3)	1.625x1.625x5	**Scan Time (min)**	15.41s/flip angle (1.1s/kz encode)
FOV (mm^3)	156x156x70	**Number of Avgs**	1
TE (ms)	0.08	**Flip Angle (°)**	8, 20, 35
TR (ms)	11.7	**Coil**	L7 + S5 + S6
Readout (ms)	0.5	**Interleaves**	105

3.6 Experiment #4: Accelerated T1-Thermometry in an Ex-Vivo Human Skull

To simulate the larger FOV requirement ($\geq$ 280 x 280 x 200 mm^3), an ex-vivo human skull was imaged. The fully sampled and under-sampled sequences were compared.

3.6.1 Methods

An ex-vivo human skull was obtained with permission from the Focused Ultrasound Foundation. Thermocouples were taped to the skull and it was placed into a bag of $75°C$ water and imaged by a 32-channel head coil as it cooled.

Table 13

UTE VIBE Sequence Parameters (3T Prisma)			
Resolution (mm)	1.578x1.578x5	**Scan Time (min)** Fully Sampled	117s/flip angle (2.65s/kz encode)
		Under Sampled (1 at center, 0.6 at edge)	59s (1.34s/kz encode)
FOV (mm^2)	202x202x176	**Number of Avgs**	1
TE (us)	80	**Flip Angle (°)**	8, 20, 35
TR (ms)	11	**Coil**	32CH head coil
Readout (ms)	0.5		

3.6.2 Results

Visually, there were minimal differences between the under sampled and normally sampled scans (**Figure 31**).

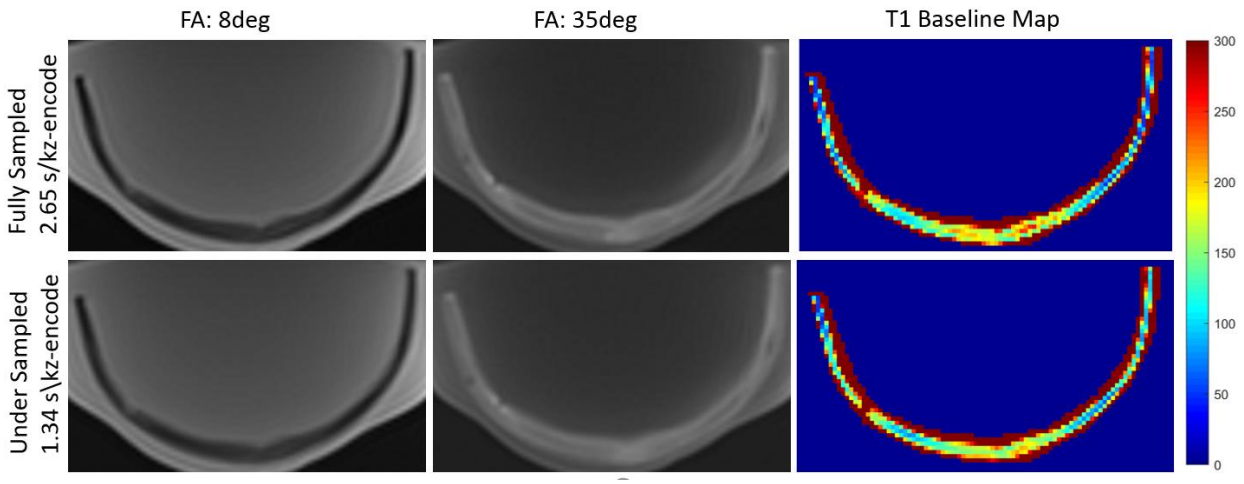

Figure 31. Acceleration with a Clinical FOV. The top row shows the fully sampled images. The bottom row shows the under-sampled images (~twice as fast). The image quality is comparable.

A water bath cooling test was performed in the skull both with and without under-sampling. The results between fully sampled and under-sampled acquisitions had some differences but generally preserved the linear trend between T1 and temperature. Within the same ROI, the baseline T1 was slightly different potentially due to a lower resolution from spiral aliasing resulting in a lower peak at the Ernst angle.

Different ROIs within the skull showed different T1 vs. temperature trends (**Figure 32**). This could be due to the porosity of the skull with pockets of water in the skull walls. Also, due to the large volume of the skull, the flip angle could vary across the skull and a flip angle correction map should be generated. The baseline T1 value was reasonable and in general either no trend or positive trends in T1 were observed. Repeating this experiment with a higher resolution as the skull is only a few pixels across and potentially with a fresher skull could improve results.

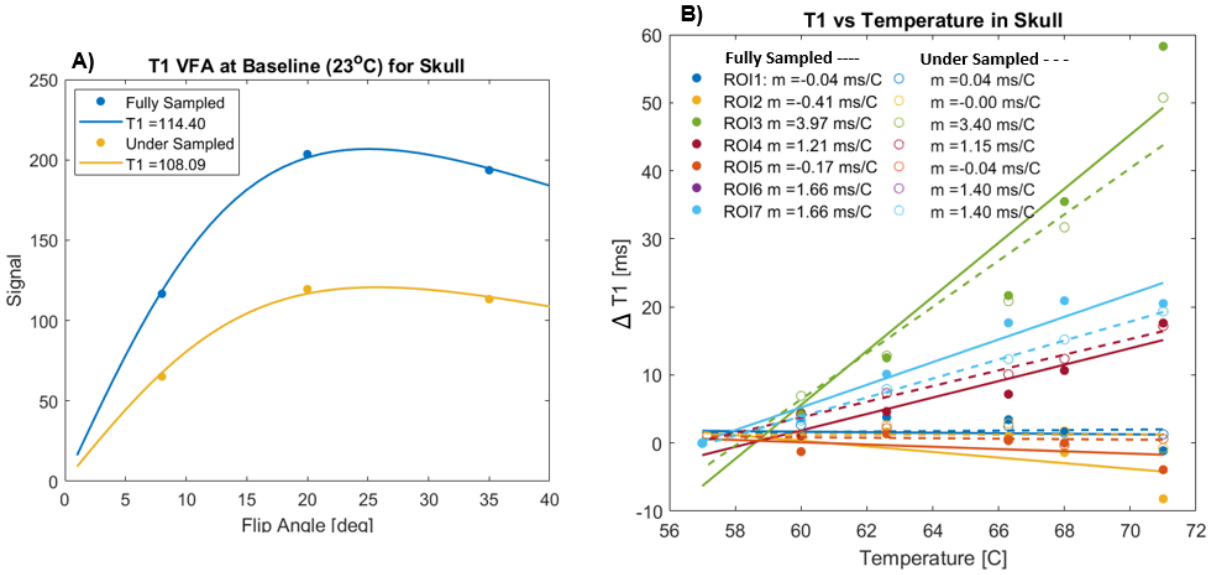

Figure 12. T1 vs. Temperature for an Ex-vivo human skull. A) Under sampling decreases the signal amplitude and slightly underestimates T1. B) The results are ROI-dependent, but T1 vs. Temperature shows a consistently positive slope of varying magnitude.

Figure 32. T1 vs. Temperature for an Ex-vivo human skull. A) Under sampling decreases the signal amplitude and slightly underestimates T1. B) The results are ROI-dependent, but T1 vs. Temperature shows a consistently positive slope of varying magnitude.

3.7 Experiment #5: FUS Localized T1-mapping

As listed in the clinical constraints (Table 1), MR bone thermometry must be able to detect localized heating caused by FUS. To test the accelerated T1 thermometry method above, the small animal FUS transducer from **2.3.1** was used.

3.7.1 Methods

Bone was cleaned from fat and marrow, drilled with a hole saw to fit the bone holder, and placed onto a ultrasound transparent film. Initially, water was poured around the bone for ultrasound conduction. However, the movement of water led to blur and other artifacts decreasing image quality. To remove these artifacts, Fomblin was used as a conductive sound medium as well as to mitigate susceptibility distortions in the bone holder. Fomblin, an inert perfluoropolyether flurocarbon, produces no MRI signal but has a similar magnetic susceptibility to tissue. It has been used previously in quantitative and high quality bone imaging by other groups [38].

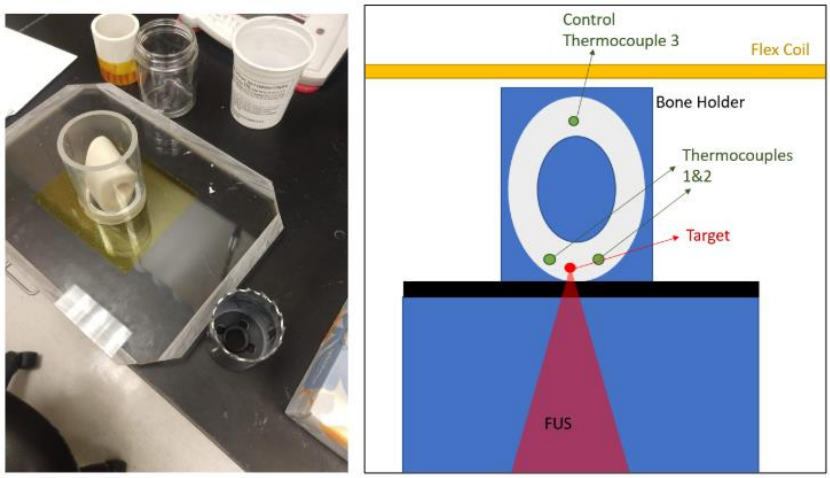

Figure 33. Localized FUS experiment setup.

A 4-channel flex coil was used for imaging as the L7 coil (which is much better) could not be used with the FUS setup; the L7 coil requires the use of a spine coil or another L7 coil, and this was not realized until after the experiment. Bone was gradually heated with 8W for 20min and imaged; however, images during sonication had strong artifacts. After reaching 53C, bone was imaged while cooling as shown in **Figure 34**.

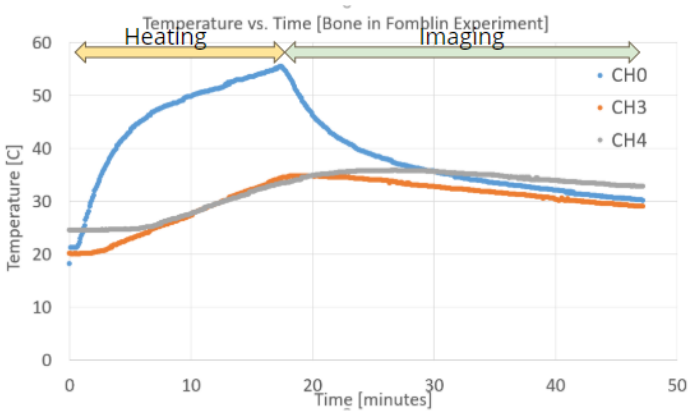

Figure 34

Table 14

UTE VIBE Sequence Parameters (3T Prisma)			
Resolution (mm)	1.8x1.8x3	**Scan Time (min)**	40s/flip angle (1.11s/kz encode)
FOV (mm^2)	221x221x108	**Number of Avgs**	1
TE (ms)	0.08	**Flip Angle (°)**	15, 25, 40
TR (s)	11	**Coil**	4-ch flex coil
Readout (ms)	0.5	**Undersampling**	1 (center), 0.7 (edge); 127 spirals

3.7.2 Results

Ultimately, we must demonstrate that localized heating can be detected for UTE VIBE T1 thermometry to be useful for clinical application. Bone was placed in Fomblin and heated with focused ultrasound with the results below. However, it was later realized that a major flip angle miscalibration was occurring as the scanner B1 tuned to the large water tank of the FUS transducer rather than the bone sample above the transducer. Therefore the T1 values of the below results are erroneous. A change in T1 was still detected (0.39ms/°C), though less than in previous experiments (0.98ms/°C). Several things could be improved with this experiment such as the use of a better coil and flip angle calibration.

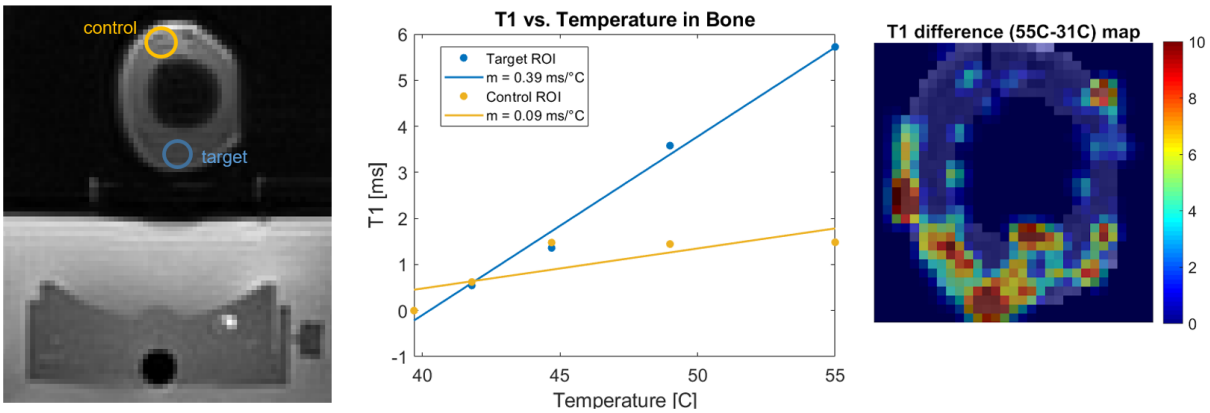

Figure 35. Localized FUS Heating Thermometry Test. A linear T1 change was detected with temperature in the target. The T1 difference map shows heating occurred at the bottom of the bone. The above data was temporally

averaged with a time window of 2 as a less optimal coil was used in this experiment than in previous water bath experiments.

3.7.3 Necessity for Manual Flip Angle Calibration

A $NiCl_2$ phantom was placed on top of an unfilled (no water) FUS transducer and imaged (left). Then the water tank was filled and the phantom was imaged again. The T1 decreased significantly (**Figure 36**). The reference voltage was compared between the (no water tank) FUS setup (255V) and (water) FUS setup (201V); the difference in reference voltage indicated a different B1 calibration readjusted for the water tank which is in turn maladjusted for the bone. Manual RF calibration is thus needed to tune the B1 transmit for the phantom or bone.

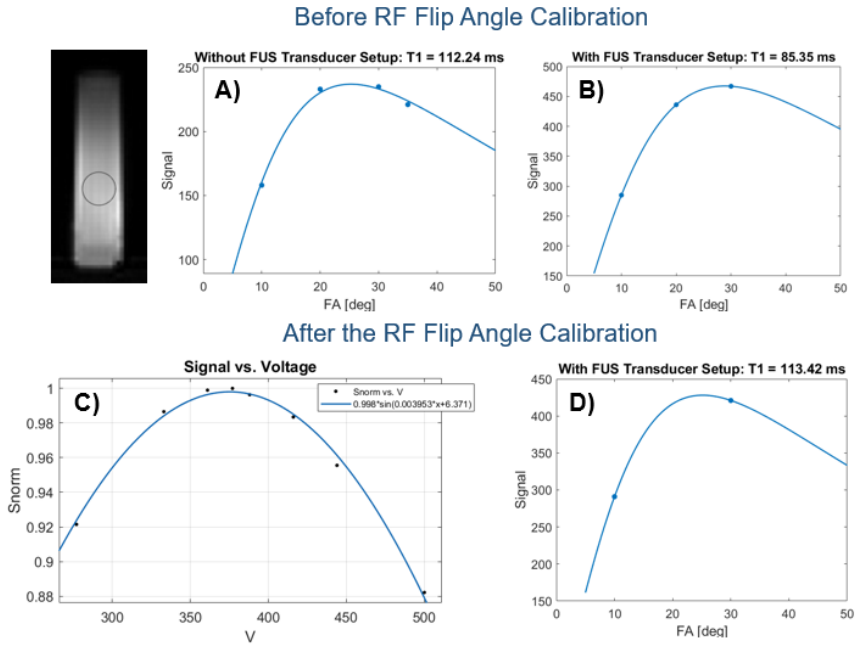

Figure 36. (A-B) Without the FUS water tank (filled), the T1 value is close to the expected $NiCl_2$ of 120ms. With the FUS water tank (filled), the T1 value decreases dramatically (erroneous). (C). The maximum of the signal corresponds to a 90° flip angle enabling the calibration of voltage to flip angle. (D) With manual flip angle calibration, the T1 value with the FUS water tank (filled) is correct.

With manual flip angle calibration (adjusted V_{ref}), the phantom's T1 was correct (the same value as without the FUS transducer). All future experiments which use the FUS transducer may require manual RF calibration if a phantom check fails.

Chapter 4 Conclusion and Future Work

4.1.1 Conclusion

MRgFUS is an important medical technology enabling high-precision non-invasive brain surgery with ultrasound. Examples of medical applications include FDA approved treatment for Parkinson's disease and essential tremor and many other disorders in the research stage such

as neuropathic pain, depression, and obsessive-compulsive disorder [39]. One challenge to treatment efficacy is posed by the skull. Its high absorption of ultrasound waves creates difficulties, one of which is skull heating. Damage from skull heating has been observed in several patients [2]. Though damage has not been shown to be harmful, it may be linked to problems such as headaches during treatment. Temperature monitoring of the skull would increase treatment safety, enable further development of MRgFUS therapy to non-central brain targets, and potentially speed up treatment by decreasing waiting time between sonications for patients. MRI based thermometry is well suited for this task as monitoring of the brain temperature is already done by MRI.

Conventional MR thermometry does not work in the skull due to its ultra-short T2, so we investigated T1-based thermometry. Skull thermometry imaging must be fast to capture heating in 90s, volumetric to detect heating anywhere in the skull, and have a short echo time (<100us) to enable the imaging of bone. It has been shown by Han et Al [3] that T1 is linear with temperature in cortical cow bone and can thus be calibrated to temperature. However, their method has not been demonstrated under clinical constraints and has a long acquisition time (8 minutes). Our initial goal was to investigate the repeatability of T1-weighted thermometry using a non-selective ultra-short-echo-time (UTE) 3D spiral sequence. First, we tested T1-weighted thermometry in simpler conditions (cooling of bone in a water bath) and then in more challenging clinically relevant conditions (heating of bone by focused ultrasound).

We found that T1-weighted thermometry was highly variable (**0**); in the water bath, bone showed either no trend or a negative linear trend (**2.2.3**), whereas in the FUS setup, bone showed an opposite trend of what was expected possibly due to B1 miscalibration leading to a lower flip angle than was prescribed and increasing T2 weighting (**2.3.2**). The variable results of T1-weighted thermometry led us to investigate T1-mapping thermometry, which depends on less factors and assumptions but takes longer (**0**). We investigated T1-mapping with a much better coil and increased resolution. Analyzing both the T1 values and the T1-weighted signal at different flip angles, we observed that the trend in T1-weighted signal is highly dependent on flip angle. Also, even with higher flip angles, T1-weighted signal is not fully linear with temperature (**3.3.2**). For the same ROIs, T1-mapping results showed a consistent linear trend (0.98 +/- 0.15ms/°C) whereas T1-weighted results showed mixed results **(3.3.2**). Thus, T1-mapping with the UTE VIBE was observed to be reliable, linear, and potentially able to be calibrated to indicate skull temperature. However, T1-mapping must be accelerated to be clinically applied. To accelerate T1-mapping, we used 6/8 partial kz sampling and changed the sampling density of the spiral interleaves using linear variable density with full sampling (1) at the center of k-space and 0.7 at the edge of k-space. The under-sampled T1 of bone cooled in a water bath still showed linear results, though the slope was higher the fully-sampled T1 of other bones (**3.3, 3.5**). Under-sampled T1-mapping was also done in ex-vivo human skull with results highly dependent on ROI due to the thinness of the skull and relatively coarse resolution.

UTE VIBE T1 mapping thermometry seems to be promising in its clinical applicability to skull monitoring, as preliminary results have shown linear measurements of T1 with temperature in contrast with the variable results of T1 weighted thermometry. However, there are still

experiments that need to be done before the UTE VIBE is demonstrated to be applicable to clinical skull thermometry.

4.1.2 Future Work

This investigation has shown that spiral volumetric T1-mapping thermometry is repeatable and reliable, and that it may be accelerated to potentially meet the clinical constraints (large FOV and short acquisition time). Rapid T1-mapping thermometry was demonstrated in bovine cortical bone, but has not been demonstrated to work with FUS-based heating under all clinical constraints; this was attempted (**3.7.2**), but the problem of B1 miscalibration was realized. Manual RF calibration combined with a double angle B1 map to check the actual flip angle should be done in the future. Several trials of localized FUS experiments with L7 coils should be done (with fat suppression and B1 mapping) on bovine bone. Then, the slope of those trials can serve as a calibration factor to convert T1 onto temperature for another "test" trial to determine method accuracy. Finally, the method can be applied to ex-vivo skull experiments, porcine head experiments, and ultimately patients.

References

[1] G. Pinton, J. Aubry, E. Bossy, M. Muller, and M. Pernot, "Attenuation , scattering , and absorption of ultrasound in the skull bone."

[2] M. L. Schwartz *et al.*, "Skull bone marrow injury caused by MR-guided focused," *J. Neurosurg.*, vol. 130, no. March, pp. 1–5, 2018.

[3] M. Han *et al.*, "Quantifying temperature-dependent T1 changes in cortical bone using ultrashort echo-time MRI," *Magn. Reson. Med.*, vol. 74, no. 6, pp. 1548–1555, 2015.

[4] D. Schlesinger, S. Benedict, C. Diederich, W. Gedroyc, A. Klibanov, and J. Larner, "MR-guided focused ultrasound surgery, present and future," *Med. Phys.*, vol. 40, no. 8, pp. 1–32, 2013.

[5] H. M. Eisenberg *et al.*, "A Randomized Trial of Focused Ultrasound Thalamotomy for Essential Tremor," 2016.

[6] P. Ghanouni *et al.*, "Transcranial MRI-guided focused ultrasound: A review of the technologic and neurologic applications," *Am. J. Roentgenol.*, vol. 205, no. 1, pp. 150–159, 2015.

[7] O. Cohen-Inbar, J. Snell, Z. Xu, and J. Sheehan, "What Holds Focused Ultrasound Back?," *World Neurosurg.*, vol. 91, pp. 661–665, 2016.

[8] N. McDannold, R. L. King, and K. Hynynen, "MRI Monitoring of Heating Produced by Ultrasound Absorption in the Skull: In Vivo Study in Pigs," *Magn. Reson. Med.*, vol. 51, no. 5, pp. 1061–1065, 2004.

[9] N. Mcdannold, P. J. White, and R. Cosgrove, "Predicting bone marrow damage in the skull af- ter clinical transcranial MRI-guided focused ul- trasound with acoustic and thermal simulations," vol. 0062, no. c, 2020.

[10] M. D. Robson, P. D. Gatehouse, M. Bydder, and G. M. Bydder, "Magnetic Resonance : An Introduction to Ultrashort," *Components*, vol. 27, no. 6, pp. 825–846, 2003.

[11] J. E. Holmes and G. M. Bydder, "MR imaging with ultrashort TE (UTE) pulse sequences: Basic principles," *Radiography*, vol. 11, no. 3, pp. 163–174, 2005.

[12] J. P. Mugler *et al.*, "Breath-hold UTE Lung Imaging using a Stack-of-Spirals Acquisition," *Proc. Int. Soc. Magn. Reson. Med.*, vol. 23, p. 1476, 2015.

[13] J. Ruan, “Investigation of the critical geometric characteristics of living human skulls utilising medical image analysis techniques Haiyan Li Zhonghua Xie Hao Wang Wengling Liu,” vol. 2, no. 4, pp. 345–367, 2007.
[14] H. Wang, M. Kim, K. P. Normoyle, and D. Llano, “Thermal regulation of the brain-an anatomical and physiological review for clinical neuroscientists,” *Front. Neurosci.*, vol. 9, no. JAN, pp. 1–6, 2016.
[15] H. Odéen and D. L. Parker, “5 Non-Invasive Thermometry with Magnetic Resonance Imaging 15.1 Introduction,” 2018.
[16] G. W. Miller, “Lecture Notes BME 8783,” Charlottesville, 2020.
[17] V. Rieke and K. B. Pauly, “MR thermometry,” *J. Magn. Reson. Imaging*, vol. 27, no. 2, pp. 376–390, 2008.
[18] P. Baron *et al.*, “In Vivo T 2 -Based MR Thermometry in Adipose Tissue Layers for High-Intensity Focused Ultrasound Near-Field Monitoring,” vol. 1064, pp. 1057–1064, 2014.
[19] X. Lu *et al.*, “Three-dimensional ultrashort echo time imaging with tricomponent analysis for human cortical bone,” *Magn. Reson. Med.*, no. February, pp. 1–8, 2019.
[20] V. Huang and W. Miller, “Rapid T2*-based MR Thermometry of Focal Heating in Cortical Bone,” in *The 18th International Symposium for Therapeutic Ultrasound*, 2018.
[21] P. Miller, S. Tafti, D. Keder, W. Miller, D. Hossainian, and W. Miller, “Towards Rapid Magnetic Resonance Thermometry in Cortical Bone,” in *The 17th International Symposium for Therapeutic Ultrasound*, 2017.
[22] B. T. Svedin and D. L. Parker, “Technical Note: The effect of 2D excitation profile on T1 measurement accuracy using the variable flip angle method with an average flip angle assumption: The,” *Med. Phys.*, vol. 44, no. 11, pp. 5930–5937, 2017.
[23] B. Lena, C. Bos, C. T. W. Moonen, M. A. Viergever, and L. W. Bartels, “Flip angle optimization and in vitro demonstration of 2D DESPOT1-based fat thermometry The whole procedure took 8 seconds per single slice (4 s for FA). In-plane FA variations were corrected using a 6 . Baron , P ., Deckers , R ., Knuttel , F . M ., Bar,” pp. 2–5, 2019.
[24] W. Miller, “Toward T1-Based Thermometry in Cortical Bone Using Ultrashort Echo-Time MRI,” *Int. Symp. Focus. Ultrasound*, no. October, p. 65–BN, 2012.
[25] W. Miller, “MR bone imaging,” *J. Ther. Ultrasound*, vol. 3, no. Suppl 1, p. O37, 2015.
[26] M. Fielden, Mugler, Miller, Pauly, “ABSTRACT: Detecting Signal Changes in Heated Bone w/3D Spiral Ultra-Short Echo Time Sequence,” p. 3867, 2014.
[27] E. Ramsay, C. Mougenot, M. Kazem, T. W. Laetsch, and R. Chopra, “Temperature-dependent MR signals in cortical bone: Potential for monitoring temperature changes during high-intensity focused ultrasound treatment in bone,” *Magn. Reson. Med.*, vol. 74, no. 4, pp. 1095–1102, 2015.
[28] H. Odeen, B. Bolster, E. K. Jeong, and D. Parker, “Investigation of temperature dependent changes in signal intensity, T1 and T2* in cortical bone,” in *ISMRM*, 2016.
[29] J. Pauly, S. Conolly, D. Nishimura, and A. Macovski, “Slice-selective excitation for very short T2 species,” in *Proceedings of SMRM*, 1989, p. 28.
[30] P. Irarrazabal and D. G. Nishimura, “Fast Three Dimensional Magnetic Resonance Imaging,” pp. 656–662.
[31] Y. Qian and F. E. Boada, “Acquisition-weighted stack of spirals for fast high-resolution three-dimensional ultra-short echo time MR imaging,” *Magn. Reson. Med.*, vol. 60, no. 1, pp. 135–145, 2008.
[32] B. T. Svedin, A. Payne, and D. L. Parker, “Simultaneous proton resonance frequency shift thermometry and T 1 measurements using a single reference variable flip angle T 1 method,” no. June 2018, pp. 3138–3152, 2019.
[33] I. L. H. Reichert *et al.*, “Magnetic resonance imaging of cortical bone with ultrashort TE pulse sequences,” *Magn. Reson. Imaging*, vol. 23, no. 5, pp. 611–618, 2005.
[34] Craig Meyer, “Rapid Magnetic Resonance Imaging,” Stanford University, 2000.

[35] A. Feinberg, D. Hale, L. Kaufman, and C. Watts, “tent ing,” pp. 527–531.
[36] C. Tsai and D. G. Nishimura, “Reduced Aliasing Artifacts Using Variable-Density k - Space Sampling Trajectories,” vol. 458, pp. 452–458, 2000.
[37] K. Thangavel and E. Ü. Saritaş, “Aqueous paramagnetic solutions for MRI phantoms at 3 T: A detailed study on relaxivities,” *Turkish J. Electr. Eng. Comput. Sci.*, vol. 25, no. 3, pp. 2108–2121, 2017.
[38] L. Wan *et al.*, “Fast quantitative 3D ultrashort echo time MRI of cortical bone using extended cones sampling,” *Magn. Reson. Med.*, no. January, pp. 1–12, 2019.
[39] Focused Ultrasound Foundation, “Overview: Status by disease category,” 2020. [Online]. Available: https://www.fusfoundation.org/?Itemid=142. [Accessed: 05-Sep-2020].
[40] D. Nishimura, *Principles of Magnetic Resonance Imaging*. 2010.
[41] M. Bernstein, *Handbook of MRI Pulse Sequences*. Elsevier Academic Press, 2004.
[42] C. Meyer, “Spiral Echo-Planar Imaging,” in *Echo-Planar Imaging*, Springer, 1996, pp. 633–658.
[43] B. M. A. Delattre, R. M. Heidemann, L. A. Crowe, J. P. Vallée, and J. N. Hyacinthe, “Spiral demystified,” *Magn. Reson. Imaging*, vol. 28, no. 6, pp. 862–881, 2010.
[44] C. H. Cunningham, J. M. Pauly, and K. S. Nayak, “Saturated double-angle method for rapid B1+ mapping,” *Magn. Reson. Med.*, vol. 55, no. 6, pp. 1326–1333, 2006.

Acknowledgements

I would like to express my gratitude for all the mentors that have taught me the physics and engineering of MRI as well as principles of physiology, signal processing, and many other important topics, and have helped me to conduct experiments, especially Dr. Craig Meyer, Dr. Wilson Miller, Dr. John Mugler, Dr. Steven Allen, and Dr. Fred Epstein. I would also like to thank all of my peers in MRI/BME at UVA for also helping me enormously with learning MRI/BME and making the journey a lot of fun.

Appendix

A1. Basics of MRI: the Signal Equation

In MRI, the data is acquired in k-space, or spatial frequency space [40]. In a scanner, and an RF pulse rotate the patient’s protons out of equilibrium which then precess about the scanner’s magnetic field. The precession causes a change in magnetic flux through a receiver coil which by Faraday’s law becomes current. If no magnetic gradients are turned on during the data acquisition, we measure the signal s(t) from the entire patient

$$s(t) = s(k_x) = \int M(x)\, e^{-i*2*\pi*k_x x}\, dx$$

Where $M(x,y,z)$ depends on the T1, T2 magnetic relaxation constants of the tissue and w_0 represents the Larmor frequency at which protons spin in the scanner. At this point, this is the same as NMR, because all we can measure about the patient is an average T1, T2. The equation that lets us jump from NMR to MRI is the Larmor equation relating the precession frequency of protons to the local magnetic field

$$\omega(x,y,z) = \gamma B_{local}(x,y,z)$$

It allows spatial position to be encoded in the frequency or phase of the protons through the use of gradients, so that for the simplified 1D case, we can see

$$\omega(x) = \gamma G_x\, x$$

$$s(t) = \int M(x)\, e^{-i\gamma G_x x * t}\, dx$$

By combining all the terms not related to the differential (dx) into one term, the detected signal s(t) is the Fourier transform of the patient's magnetization

$$s(t) = s(k_x) = \int M(x)\, e^{-i*2*\pi*k_x x}\, dx$$

where $k_x = \frac{\gamma}{2\pi} G_x t$. After measuring all the $s(k_x)$ points through time, we can determine $M(x)$ by taking the inverse Fourier transform, which is how we can reconstruct an image of the patient's body from the data:

$$M(x) = \int s(k_x)\, e^{i*2*\pi*k_x x}\, dk_x$$

The Fourier transform is a linear operation; so if we want to reconstruct the patient using 128 x 128 pixels in x,y, we need to collect the corresponding 128 x 128 k_x,k_y data. Typically this is done using Cartesian sampling, as this is the most straightforward sampling method. In principal though, we can sample the k-space in any way, as long as we meet one requirement: the Nyquist sampling frequency, Δk. The Nyquist criteria in MRI can be derived in many ways (more rigorous than the below) but the following relationship shows it well.

$$F\big(f(x) ** g(x)\big) = F\big(f(x)\big)F\big(g(x)\big) = F(k_x)F(k_g)$$

The convolution theorem states that the Fourier transform of the convolution of two functions is equivalent to the Fourier transform of each function in the corresponding domain. By sampling in MRI, we are multiplying the continuous frequency space by a comb function (a string of delta functions which sifts values) $F(k_x)\text{Ш}(k_x)$), which by the convolution theorem becomes

$$F\big(f(x) ** \text{Ш}(x)\big) = F(k_x)\frac{1}{\Delta k_x}\ \text{Ш}(\frac{k_x}{\Delta k_x}))$$

A convolution with the $\text{Ш}(x)$ function, means f(x) is replicated with the period of $\frac{1}{\Delta k_x}$ so if the sampling period is too low, the object of size L will overlap with itself in the final image ($\frac{1}{\Delta k_x} \geq L$) . Thus, $\Delta k_{x,y,z} \leq \frac{1}{L}$ to avoid overlap. There are many ways to or "travel" through k-space while meeting the Nyquist limit, each with their own advantages and disadvantages.

A2. Spiral MRI

Spiral Sampling Requirement

It helps to first go over radial sampling, before delving into spiral sampling requirements. In the r-hat direction, the requirement is the same as in Cartesian space, because each radial line is like a rotated k_y line: $k_r = \frac{1}{L}$ [41]. However, it is different in the azimuthal direction, in which $k_{max}\Delta\phi \leq \frac{1}{L}$ because that is the maximum distance between each spoke. In the Cartesian method, we could see the needed frequency by finding (using convolution theorem)

$$\text{Ш}(k_x, k_y)M(k_x, k_y) = \text{Ш}(x, y) ** M(x, y)$$

which requires taking the Fourier transform of $\text{Ш}(k_x, k_y)$. In the radial case, that would be less simple, because the radial Fourier transform is more complex to do on a radial Ш function (also called Hankel transform)

$$F_v(k) = \int_0^\infty f(r)J_v(kr)r * dr$$

where $J_v(kr)$ is a v-order Bessel function. Just like in radial sampling, to avoid aliasing, spiral sampling must have 1/L separation azimuthally and radially. The trajectory of an Archimedean spiral (radius k, proportional to azimuthal angle, θ) is [42]

$$k(t) = \lambda\theta(t)$$

where λ is a constant. From this equation, the radial distance k(t) is $2\pi\lambda$ as $\theta(t)$ advances through 2π. If there are N interleaves, then the radial distance at any azimuthal angle is $\Delta k = 2\pi\lambda/N_{shot}$. As the Nyquist requirement is $\Delta k = \frac{1}{L}$, $\lambda = N_{shot}/(2\pi L)$ to avoid aliasing [41]. Thus, it is up to the user to choose N_{shot}, L, and k(t) max (resolution). Then, the rate at which k-space is sampled via spiral ($\theta(t)$) is decided, dependent on the gradient waveforms with the linear velocity proportional to:

$$G_0 = \sqrt{G_x(t)^2 + G_y(t)^2}$$

To meet the Nyquist requirement, $\Delta k_{azimuthal} = \frac{\gamma}{2\pi} G_0 T_{samp} = 1/L$ where T_{samp} is chosen based on the receiver BW (hardware constraint), $\Delta v = \frac{1}{T_{samp}/2}$. The resolution dictates the necessary, k_{max}, where $k_{max} = \frac{N}{2L}$ and $N = L/\Delta x$. So knowing L (FOV) and desired resolution, N (effective) can be calculated and k_{max} determined.

Calculating Spiral Gradients

In order to move through k-space, we must play different gradients

$$k(t) = \int_0^t G(t')\, dt'$$

Thus, $G = \frac{d}{dt} k(t)$. Then, we solve G(t) in terms of the Cartesian components [41]

$$k_x(t) = \lambda\theta(t) * \cos\big(\theta(t)\big);\ k_y(t) = \lambda\theta(t) * \sin(\theta(t))$$

$$G_x = \frac{2\pi}{\gamma}\ \lambda\dot{\theta}\ (cos\theta - \theta\sin(\theta));\ G_y = \frac{2\pi}{\gamma}\ \lambda\dot{\theta}\ (sin\theta + \theta\cos(\theta));$$

And the slew rate, which is important because there is a hardware limitation on how fast the gx and gy can change is given by d/dt(Gx) and d/dt(Gy).

The gradient and slew magnitudes are then $G(t) = \sqrt{(\ G_x^2 + G_y^2)} = \frac{2\pi}{\gamma}\lambda\dot{\theta}\sqrt{1+\theta^2}$ and similary, $S_R(t) = \frac{2\pi}{\gamma}\lambda\left[\left(\ddot{\theta} - \theta\dot{\theta}^2\right)^2 + \left(2\dot{\theta}^2 + \theta\ddot{\theta}\right)^2\right]^{1/2}$ [41]

The constraint would be $S_R(t) = S_{R,0}$ (G(t)<G0) and G(t) = G0 thereafter.

The equations above can be combined into one differential equation

$$\ddot{\theta}(t) = \frac{f\big(\theta,\dot{\theta}\ \big) - \theta\dot{\theta}^{\ 2})}{1+\theta^2}$$

Where $f\big(\theta,\dot{\theta}\ \big) = \left((\frac{\gamma}{2\pi} * \frac{S_{R0}}{\lambda})^2(1+\theta^2) - \dot{\theta}^{\ 4}(2+\theta^2)^2\right)^{1/2}$ if G < G0 and 0 otherwise.

The initial conditions are $\theta(0) = 0,\ \dot{\theta}(0) = 0,\ \ddot{\theta}(0)\ = \gamma * \frac{S_{R0}}{\lambda}$ (plugging in t=0 into equations above after setting $\theta(0) = 0$.

A challenge of spiral MRI is that the above DFQ does not have an analytical solution without doing approximations. Thus, designing a trajectory with this method makes real-time MRI challenging as the user changes parameters forcing the scanner software to calculate the necessary gradients, which may be computationally intensive. Current spiral k-space trajectory planning involve the use of some approximations [43].

A3. B1 Flip Angle Map

While the Variable Flip Angle method is faster than others, it requires accurate flip angles, which is a big problem for 2D (slice selective) MRI due to the non-uniform slice profile resulting in a flip angle variation at large flip angles as can be seen from the Bloch equation solution. However, in non-selective MRI, the slice profile and flip angles are more uniform thus making 3D VFA more practical. However, if there are transmit field (B_1) variations, the actual flip angle may still vary from the prescribed flip angle.

B_1 inhomogeneity is caused by the dielectric and conductive properties of the material being imaged in the coil (B_1 penetration) as well as the transmitting coil geometry. When the B_1 or RF

wavelength is comparable to the size of the object, standing waves can occur causing a variation in B_1. There are many ways to correct for B_1 inhomogeneity by estimating B_1 from a pulse sequence which varies with respect to the B_1 field.

The GRE dual-angle method (GRE-DA) uses the magnitude of two images [44]:

$$m_1 = M_o e^{-\frac{TE}{T_2^*}} \frac{(1-E_1)\sin(\theta)}{(1-E_1\cos(\theta))}$$
$$m_2 = M_o e^{-\frac{TE}{T_2^*}} \frac{(1-E_1)\sin(2\theta)}{(1-E_1\cos(2\theta))}$$

To form the ratio

$$\frac{m_1}{m_2} = \frac{\sin(\theta)}{(1-E_1\cos(\theta))} * \frac{(1-E_1\cos(2\theta))}{\sin(2\theta)}$$

If T1 relaxation can be neglected ($TR \geq 5\,T_1$), then $\frac{m_1}{m_2} = \frac{1}{2\cos(\theta)}$ so that the actual θ can be calculated. Though this method is slow, it is straightforward to implement in the UTE VIBE (TR = 600 ms) and can be validated by comparing the UTE VIBE dual angle results with a standard method already implemented on the scanner in a water phantom.

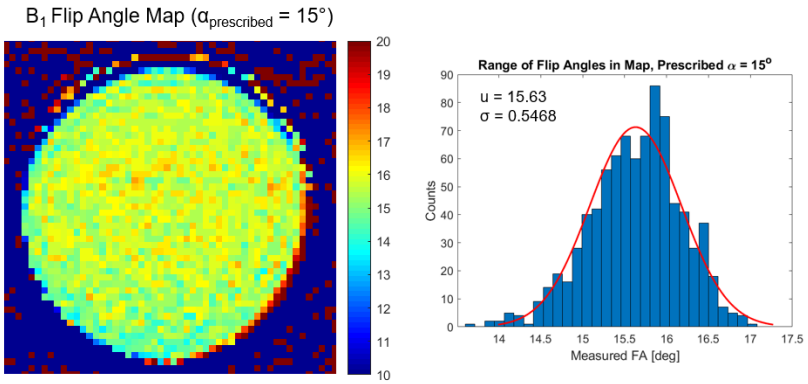

Figure 37. Example of a UTE VIBE flip angle map of a phantom.